ARTICLE

doi:10.1038/nature14323

MAP4K4 regulates integrin–FERM binding to control endothelial cell motility

Philip Vitorino[1], Stacey Yeung[1], Ailey Crow[1], Jesse Bakke[2], Tanya Smyczek[1], Kristina West[3], Erin McNamara[3], Jeffrey Eastham-Anderson[4], Stephen Gould[3], Seth F. Harris[5], Chudi Ndubaku[6] & Weilan Ye[1]

Cell migration is a stepwise process that coordinates multiple molecular machineries. Using *in vitro* angiogenesis screens with short interfering RNA and chemical inhibitors, we define here a MAP4K4–moesin–talin–β1–integrin molecular pathway that promotes efficient plasma membrane retraction during endothelial cell migration. Loss of MAP4K4 decreased membrane dynamics, slowed endothelial cell migration, and impaired angiogenesis *in vitro* and *in vivo*. In migrating endothelial cells, MAP4K4 phosphorylates moesin in retracting membranes at sites of focal adhesion disassembly. Epistasis analyses indicated that moesin functions downstream of MAP4K4 to inactivate integrin by competing with talin for binding to β1–integrin intracellular domain. Consequently, loss of moesin (encoded by the *MSN* gene) or *MAP4K4* reduced adhesion disassembly rate in endothelial cells. Additionally, α5β1–integrin blockade reversed the membrane retraction defects associated with loss of *Map4k4 in vitro* and *in vivo*. Our study uncovers a novel aspect of endothelial cell migration. Finally, loss of MAP4K4 function suppressed pathological angiogenesis in disease models, identifying MAP4K4 as a potential therapeutic target.

Cell migration relies on coordinated engagement and disengagement of cell–extracellular matrix interactions[1]. Integrin receptors bind extracellular matrix ligands and orchestrate cytoskeletal and signalling changes[2]. The affinity of integrins for extracellular matrix ligands increases when they bind FERM (4.1 protein, ezrin, radixin, moesin) domain-containing proteins such as talin[3]. Once engaged, integrins cluster into nascent focal complexes and recruit additional proteins, maturing into long, stable focal adhesions (FAs). As cells migrate, stable FAs disassembled to enable membrane retraction[4].

MAP4K4 and its invertebrate orthologues belong to the Ste20 family kinases[5], which are broadly expressed and affect many biological processes, including embryonic development[6,7] and inflammation[8]. MAP4K4 regulates multiple molecular pathways in a context-dependent manner[9–12], including integrin biology through unknown mechanisms[13,14].

Moesin, ezrin, and radixin comprise the ERM protein family (ERMs) and are substrates of MAP4K4[12]. Like talin, ERMs contain an amino-terminal FERM domain that binds transmembrane proteins and a carboxy-terminal tail that binds actin. Upon phosphorylation, the two domains dissociate and form a tether between actin and the plasma membrane to regulate cell–cell adhesion, endocytosis, cell polarity, and mitosis[15]. ERMs localize to retracting membranes in different cell types[16,17], but their role in this context remains unknown.

Here we report the discovery of a novel molecular pathway that regulates endothelial cell motility. MAP4K4 phosphorylates moesin, which displaces talin from INTβ1 to inactivate β1-integrin and promote FA disassembly, thereby enabling membrane retraction during endothelial cell migration. We developed chemical inhibitors against MAP4K4 that suppress pathologic angiogenesis *in vivo*, revealing a new opportunity to inhibit pathologic angiogenesis.

MAP4K4 enhances endothelial cell membrane retraction

We used a human umbilical vein endothelial cell (HUVEC) sprouting assay in three dimensional (3D) culture (Extended Data Fig. 1a) to screen chemical inhibitors against known targets. We found that GNE-220, a potent and selective inhibitor of MAP4K4 (Supplementary Table 1), altered HUVEC sprout morphology. On day 1, GNE-220 shifted the distribution of subcellular protrusion towards longer lengths (>40 μm) and increased total protrusions (Fig. 1a, b, Extended Data Fig. 1b–e, Supplementary Videos 1 and 2). Furthermore, control samples formed well-defined sprouts with multiple endothelial cells (red arrows, Fig. 1a), whereas GNE-220 induced wide and short aberrant structures (red arrowheads, Fig. 1a), probably owing to increased encounter of endothelial cell membrane protrusions between adjacent sprouts (Supplementary Videos 1 and 2). Control sprouts grew in length over time, but the GNE-220 treated structures were significantly shorter than the control sprouts (Fig. 1a, c). Since GNE-220 also inhibits a few other kinases (Supplementary Tables 1 and 2), we confirmed that the phenotype of GNE-220 was mediated by MAP4K4 inhibition by using individual and pooled siRNA against *MAP4K4* (*siMAP4K4*) and found that knockdown phenocopied GNE-220 treatment (Fig. 1a, b, Extended Data Fig. 1f, g). Knockdown with *siMAP4K4* did not alter levels of the closely-related kinases MINK, TNIK, and MAP4K5, nor did knockdown of these MAP4Ks phenocopy *siMAP4K4* (Extended Data Fig. 1h–j).

Although GNE-220 reduced sprout length, the cell numbers and proliferation remained unchanged (Fig. 1c, Extended Data Fig. 2a–c), implying that reduced migration, but not proliferation, delays sprout outgrowth. Consistent with a migration defect, GNE-220 and *siMAP4K4* reduced HUVEC scratch wound closure (Extended Data Fig. 2d). Since inhibition of the DLL4–Notch pathway also alters HUVEC sprout[18], we compared MAP4K4 versus Notch inhibition. While Notch inhibition increased endothelial cell numbers and proliferation, it did not increase subcellular protrusions (Extended Data Fig. 2a–c, e, f). Furthermore, MAP4K4 knockdown did not alter filopodia dynamics (Supplementary Video 3, Extended Data Fig. 2g), indicating that MAP4K4 and NOTCH have different functions.

We quantified membrane dynamics by time-lapse imaging of HUVEC sprouts with fluorescently labelled membranes and nuclei. Control sprouts exhibited frequent membrane protrusion, retraction, and

[1]Molecular Biology Department, Genentech, Inc., South San Francisco, California 94080, USA. [2]Chemical Biology and Therapeutics Department, St Jude Children's Research Hospital, Memphis, Tennessee 38105, USA. [3]Translational Oncology Department, Genentech, Inc., South San Francisco, California 94080, USA. [4]Pathology Department, Genentech, Inc., South San Francisco, California 94080, USA. [5]Structural Biology Department, Genentech, Inc., South San Francisco, California 94080, USA. [6]Discovery Chemistry Department, Genentech, Inc., South San Francisco, California 94080, USA.

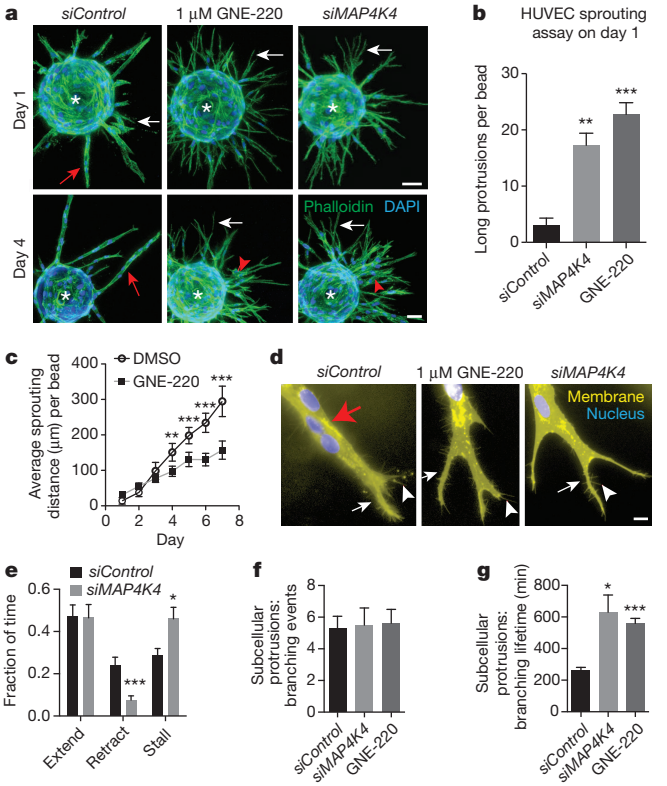

Figure 1 | MAP4K4 regulates endothelial cell membrane dynamics. **a**, Day 1 and day 4 HUVEC sprouting 3D culture treated with siRNA or GNE-220 and stained with phalloidin (green) and DAPI (blue). Scale bars, 50 μm. **b**, Long protrusions (>40 μm) per bead from 1-day cultures. Each bar represents mean of four experiments, >10 beads per experiment. **c**, Average sprout lengths per bead over time. >10 beads per condition, representative of three experiments. **d**, HUVEC sprouts expressing Lck–RFP (yellow), stained with Hoechst-33342 (blue), and treated with the indicated agents. Scale bar, 10 μm. **e**–**g**, Quantification of subcellular protrusions dynamics (**e**), branching events (**f**), and branching lifetime (**g**) from time-lapse videos. **e**, 13 sprouts per condition, representative of 3 experiments. **f**, **g**, Representing >8 sprouting event per condition, each sprouting event contained >40 branching events. **a**, **d**, Normal sprouts (red arrows), aberrant structures (red arrowheads), subcellular protrusions (white arrows), filopodia (white arrowheads) and beads (asterisks). For all figures, error bars represent standard error of the mean (s.e.m.); statistical significance between the indicated sample versus control or between the marked pairs are $*P < 0.05$, $**P < 0.01$, $***P < 0.001$, or NS, not significant ($P \geq 0.05$); statistical analysis methods are described in the Methods section.

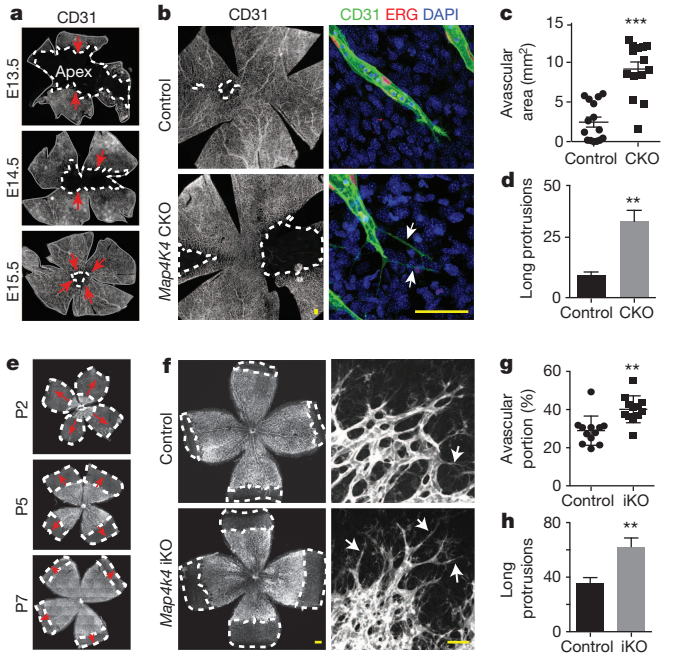

Figure 2 | *Map4k4* is essential for vascular development. **a**, Flat-mounted head skins immunologically stained for CD31 at the indicated embryonic stages. **b**, E15.5 head skins immunologically stained for the indicated markers (CD31 for endothelial cell, ERG for endothelial cell nuclei) and DAPI for all nuclei. Left, low magnification images. Right, close-up of tip cells with long membrane protrusions apparent in the bottom panel (arrows). **c**, Avascular areas in E15.5 head skins. Fifteen embryos for control, 14 embryos for CKO. Representative of 3 experiments, each experiment contained multiple litters of mice. **d**, Number of long membrane protrusions (>40 μm) along the vascular edge per mm length of vascular edge. Eight embryos per genotype, representative of 2 experiments, each experiment contained multiple litters of mice. **e**, Flat-mounted retinas stained for isolectin-B4 (vascular marker) at the indicated postnatal stages (P). **f**, P7 retinas with the indicated genotypes stained for isolectin-B4. Left, low magnification images. Right, close-up of tip cells with long membrane protrusions (arrows). **g**, Avascular area normalized to total retina areas. Twelve mice per genotype, representative of 3 experiments, each experiment contained multiple litters of mice. **h**, Numbers of long membrane protrusions (>40 μm) along the vascular front per centimetre of vascular front. Six mice for control, 7 mice for iKO, the entire circumference of each retina was quantified. Representative of two experiments, each experiment contained multiple litters of mice. Dotted lines demark avascular areas. Red arrows indicate direction of vascular growth. Scale bars, 50 μm.

bifurcation (Supplementary Video 3, Fig. 1d). With *MAP4K4* knockdown or inhibition, endothelial cells accumulated long, thin subcellular protrusions (Fig. 1d) owing to reduced retraction frequency and increased stalling frequency of these protrusions (Figs 1e, 3c). We also quantified branching events in the subcellular protrusions over 16 h. *MAP4K4* knockdown or inhibition did not change branching frequency but increased protrusion lifetime (Fig. 1f, g), suggesting that the failure to retract results in the accumulation of normally transient membrane protrusions.

MAP4K4 regulates vascular development *in vivo*

Map4k4 knockout (KO) caused embryonic lethality at embryonic day 9.5 (E9.5) due to mesodermal patterning defects[7]. To assess the role of MAP4K4 in vascular development, we generated a floxed allele of *Map4k4* (*Map4k4*$^{fl/fl}$) (Extended Data Fig. 3a) and crossed it to Tie2-Cre mice to induce endothelial cell conditional knockout (CKO). Loss of transcription of the sequence encoded by *Map4k4* exon 6 in embryonic endothelial cells was confirmed (Extended Data Fig. 3c). Heterozygous CKOs had no apparent defect. However, no live homozygous CKOs (*Map4k4*$^{cko/cko}$) were born, suggesting embryonic lethality (Extended Data Fig. 3b).

Analysis of E9.5–E17.5 embryos found no apparent defect in *Map4k4*$^{cko/cko}$ embryos up to E13.5 (data not shown). At E14.5, ~95% of *Map4k4*$^{cko/cko}$ embryos had multifocal oedema and haemorrhage; at E15.5, haemorrhage and oedema were systemic in all *Map4k4*$^{cko/cko}$ embryos, culminating in lethality by E16.5 (Extended Data Fig. 3d). We then examined vascular patterns in the head skins because vessels grow from the periphery towards the apex of the skull in a stereotypic pattern between E13 and E15 (Fig. 2a). At E15.5, while the head skin in control embryos had little avascular area, large avascular areas were apparent in *Map4k4*$^{cko/cko}$ embryos, suggesting delayed vascular development (Fig. 2b, c). Although vessel coverage was delayed in *Map4k4*$^{cko/cko}$ head skins, endothelial cell number and proliferation were unaffected (Extended Data Fig. 3e–g), implicating defective endothelial cell migration. In addition, CKO vessels near the vascular front accumulated long subcellular protrusions (Fig. 2b, d, Extended Data Fig. 3h, i), recapitulating the *in vitro* phenotype. Examination of cell–cell junctions with VE-cadherin staining revealed no difference between control and CKO

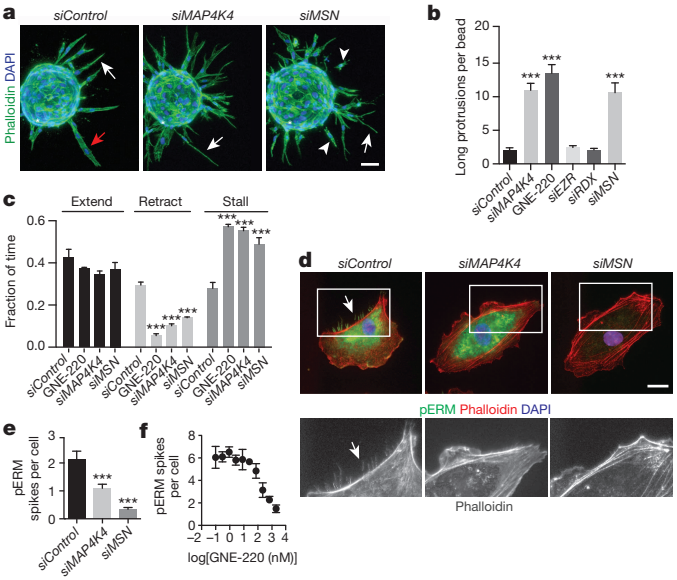

Figure 3 | MAP4K4 and moesin regulate membrane retraction. **a**, HUVEC sprouts from cells transfected with the indicated siRNAs after 1 day in culture. Arrows and asterisks defined as in Fig. 1a. Arrowheads indicate fragmented sprouts. Scale bar, 50 μm. **b**, Long protrusions (>40 μm) per bead from HUVEC sprouting cultures treated with pooled siRNAs targeting the indicated genes. *EZR*, ezrin; *MSN*, moesin; *RDX*, radixin. Each bar represents mean of 4 experiments, >10 beads per experiment. **c**, Quantification of membrane dynamics over a 16-h period in HUVEC sprouts treated with the indicated agents. Each bar represents mean of four beads, >15 sprouts per bead. Representative of 3 experiments. **d**, HUVEC transfected with the indicated siRNA were stained with phalloidin (red in top panels, white in bottom panels), pERM (green), and DAPI (blue). Bottom panels are enlarged views of the boxed regions. Scale bar, 20 μm. Arrow indicates retraction fibres. **e**, Quantification of pERM-positive retraction fibres in HUVEC transfected with the indicated siRNA. Means of 3 experiments, >500 cells per experiment. **f**, Dose–response curve of GNE-220 on pERM-positive spikes. Line shows best-fit, variable slope response curve. Four biological replicates, >100 cells per replicate, representative of 2 experiments.

animals (Extended Data Fig. 4a, b). Furthermore, MAP4K4 knockdown or inhibition did not alter permeability in HUVEC cultures (Extended Data Fig. 4c).

We then examined the postnatal retinal vasculature, which also develops in a stereotypic manner[19] (Fig. 2e). One-day-old pups (P1) born from *Map4k4*$^{fl/fl}$::Rosa26.CreERT2 mice were injected with tamoxifen to induce *Map4k4* KO (iKO) (Extended Data Fig. 4d). Like the embryonic head skin, P7 *Map4k4*$^{iKO/iKO}$ retinal vessels exhibited delayed outward migration and accumulation of long membrane protrusions without change in endothelial cell proliferation (Fig. 2f–h, Extended Data Fig. 4e, f) nor pericyte coverage (Extended Data Fig. 4g, h), further indicating that *Map4k4* regulates endothelial cell migration.

Moesin mediates the membrane retraction effect of MAP4K4

To identify substrate(s) of MAP4K4 in endothelial cells, we performed a siRNA screen targeting 60 candidates, including all MAP3Ks and factors involved in cell migration and membrane dynamics. Moesin emerged as a strong candidate because pooled or individual *MSN* siRNAs phenocopied MAP4K4 inhibition (Fig. 3a, b, Extended Data Fig. 5a, b). Although moesin is closely related to radixin and ezrin, *siMSN* alone was sufficient to phenocopy *siMAP4K4* (Fig. 3b), possibly owing to its higher expression in endothelial cells[20]. Time-lapse analysis showed that *siMSN* reduced retraction frequency with a concomitant increase in membrane stalling (Fig. 3c), similar to *siMAP4K4*. Unlike *siMAP4K4*, *siMSN* also caused sprout fragmentation (Fig. 3a, arrowheads), likely due to a MAP4K4-independent function[15].

Phosphorylation at threonine 558 (T558) activates moesin[15]. Consistent with a previous report[12], we found that recombinant MAP4K4 phosphorylates recombinant moesin (Extended Data Fig. 5c, d). Because western blot of HUVEC lysates revealed only a marginal reduction in phospho-ERM (pERM) in *MAP4K4* knockdown HUVEC versus control (Extended Data Fig. 5e), we examined pERM distribution in HUVEC by immunofluorescence staining. Control cells contain two pools of pERM: one in the cell centre, and one in clustered fibres at the cell periphery (Fig. 3d). In time-lapse images, these clustered fibres were associated with retracting but not extending membranes (Supplementary Video 4), and therefore were defined as retraction fibres. While *siMSN* reduced all pERM, *siMAP4K4* only affected pERM in the retraction fibres (Fig. 3d, e). Actin staining revealed a lack of retraction fibres in the *MAP4K4* and *MSN* knockdown cells (Fig. 3d, bottom panels), suggesting that localized ERM phosphorylation is required for the formation of retraction fibres. GNE-220 also reduced pERM^{+} retraction fibres in a dose-dependent manner (Fig. 3f). These data suggest that MAP4K4 is required for ERM phosphorylation in retracting membranes.

MAP4K4 and moesin regulate FA disassembly

Membrane retraction occurs through the coordination of actomyosin contraction and FA disassembly[1]. As the level and distribution of p-myosin were similar in control, *MAP4K4* knockdown or GNE-220-treated HUVEC (Extended Data Fig. 6a, b), we investigated whether cell–extracellular matrix attachments were altered by *siMAP4K4* or *siMSN*. Since β1-integrin plays an important role in vascular development[21,22], we examined INTβ1 in endothelial cells. Staining of active INTβ1 showed an increase in the number of long FAs (Fig. 4a, b, Extended Data Fig. 6c, d) but no obvious change in nascent FAs marked by INTβ3 or INTαVβ5 (Extended Data Fig. 6d, e). Paxillin, a FA-associated protein, showed a similar phenotype (Extended Data Fig. 6e). GNE-220 also dose-dependently increased the number of active-INTβ1^{+} long FAs (Fig. 4c). Since cell–extracellular matrix adhesion in 2D and 3D contexts can vary[23], we stained active INTβ1 in HUVEC sprouts.

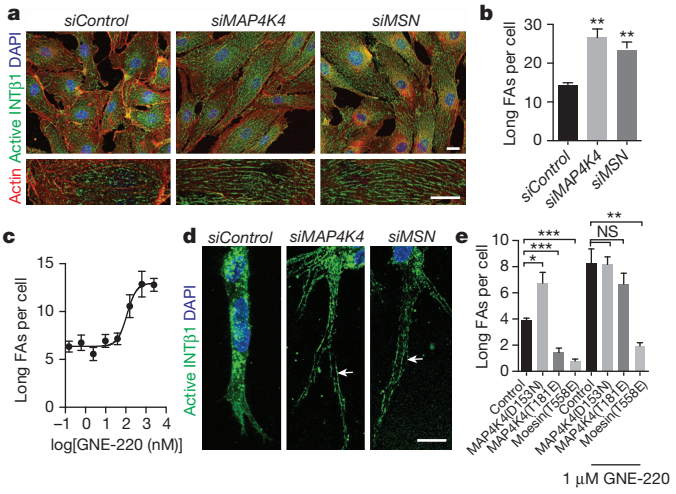

Figure 4 | MAP4K4 and moesin regulate FA length. **a**, Confocal images of HUVEC transfected with the indicated siRNA and stained for active INTβ1 (green) and with phalloidin (red) and DAPI (blue). Bottom panels, close-up views. **b**, Numbers of long FAs (defined in the Methods) per cell in HUVEC cultured for 3 days after siRNA transfection. Means of 3 experiments, 3 replicates per condition in each experiment, >500 cells per replicate. **c**, GNE-220 dose-dependently increased long FA numbers per cell on HUVEC after 18 h of treatment. Four biological replicates, >500 cells per replicate, representative of 3 experiments. **d**, HUVEC sprouts in 3D stained for active INTβ1 (green) and with DAPI (blue). Arrows indicate long adhesions. **e**, Long FA numbers per cell in HUVEC stably expressing mutated MAP4K4 or moesin in the presence or absence of GNE-220. Four biological replicates, > 500 cells per replicate, representative of 2 experiments. Scale bars, 20 μm.

siMSN or *siMAP4K4* also increased long adhesions located within subcellular protrusions in 3D (Fig. 4d).

To investigate the epistatic relationship between MAP4K4 and moesin, we evaluated the effect of gain-of-function and loss-of-function mutations of these proteins. Overexpressing kinase-dead MAP4K4 (D153N) increased long FAs to a similar extent as *siMAP4K4* or GNE-220 (Fig. 4b, c, e). Conversely, overexpressing phospho-mimetic mutants of MAP4K4(T181E) or moesin(T558E) reduced long FAs (Fig. 4e). GNE-220 restored long FAs in cells expressing MAP4K4(T181E) but had little effect on cells expressing moesin(T558E), suggesting that moesin acts downstream of MAP4K4 (Fig. 4e). Additionally, wild-type moesin, but not mutant moesin(T558A), restores FA length in *MSN* knockdown cells, suggesting that phosphorylation is critical for the effect of moesin on FAs (Extended Data Fig. 6f, g).

Although ERM localization to retraction fibres was reported[24], the relationship between retraction fibres and FAs has not been established. To explore this relationship, HUVEC with green-fluorescent-protein-labelled mature FAs (tensin–GFP[4]) and membrane tracker were monitored with time-lapse imaging. Retraction fibres trailed immediately behind receding FAs, suggesting that retraction fibres mark sites of adhesion disassembly (Fig. 5a). Interestingly, pERM accumulated in the retraction fibres distal to the active INTβ1 without marked overlap (Fig. 5b), suggesting that the accumulation of pERM may be incompatible with the maintenance of active INTβ1 in the retraction fibres.

We next examined the distribution of haemagglutinin (HA)-tagged MAP4K4 and found it to be broadly distributed and present in retraction fibres (Extended Data Fig. 7a). It is possible that MAP4K4 activation rather than localization may account for its localized activity.

FA disassembly was measured by live-imaging of HUVEC expressing the FA markers tensin–GFP or paxillin–GFP[4]. While control cells exhibited extensive membrane retraction coincident with rapid FA disassembly, cells treated with GNE-220, *siMSN*, or *siMAP4K4* had similar FA assembly rates but much reduced FA disassembly rates, resulting in increased FA decay time (Fig. 5c, d, Extended Data Fig. 7b, c, Supplementary Video 5). These data demonstrate that MAP4K4 and moesin promote FA disassembly in retraction fibres, which may be achieved by either turnover or inactivation of surface INTβ1. To distinguish these two possibilities, we compared the distribution of pERM to total and active INTβ1 in retraction fibres. Unlike active INTβ1, total INTβ1 and pERM overlapped in retraction fibres (Extended Data Fig. 7d), suggesting that pERM is likely to regulate the activation rather than the level of INTβ1.

Moesin inactivates INTβ1 by suppressing talin binding

Talin-FERM domain activates INTβ1 by binding its intracellular domain (β1ICD)[3]. Similar to active INTβ1, talin and pERM were mostly non-overlapping in retraction fibres (Extended Data Fig. 7e). Because moesin and talin share similar protein domains, we tested if the FERM domain of moesin may displace talin-FERM from β1ICD to inactivate INTβ1. We measured integrin activation by FACS with a labelled peptide derived from fibronectin. As expected, expression of mCherry–talin-FERM fusion protein in CHO cells increased active INTβ1 (Fig. 5e). Overexpression of Venus–moesin-FERM fusion protein inactivated INTβ1 with or without exogenously expressed talin (Fig. 5e), suggesting that moesin-FERM inhibits talin-mediated integrin activation. Total integrin was moderately affected by talin and moesin expression, possibly as an indirect consequence of altered activation (data not shown). Unlike moesin-FERM, the FERM domain from the band4.1 protein did not inactivate INTβ1 (Extended Data Fig. 7f).

We then tested if moesin-FERM may compete with talin for binding to β1ICD. His-tagged β1ICD, but not a binding-deficient mutant β1ICD or an unrelated protein RKIP, was able to pull-down talin-FERM (Fig. 5f). Incubation of β1ICD with increasing levels of moesin-FERM showed dose-dependent binding that coincided with reduced talin association regardless of whether talin-FERM was added after (Fig. 5f, g) or before (Extended Data Fig. 7g, h) moesin-FERM. Conversely, talin

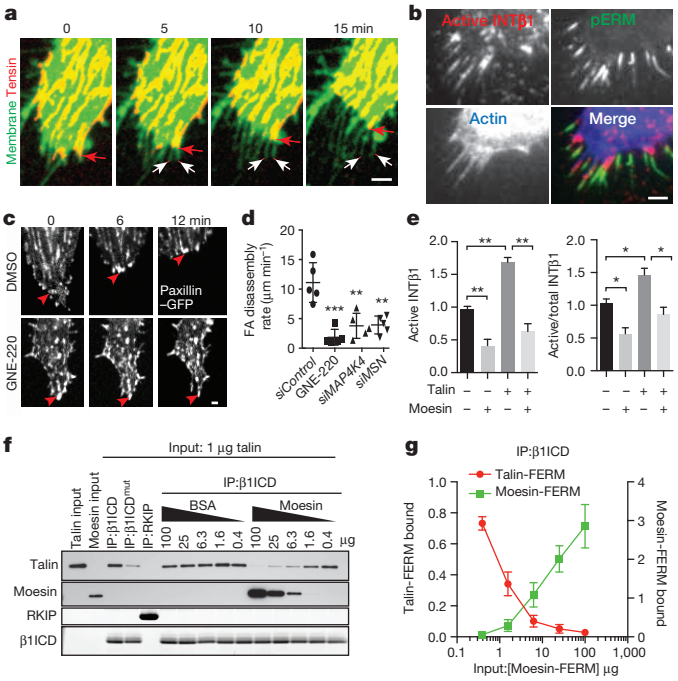

Figure 5 | MAP4K4 and moesin promote FA disassembly. **a**, Time lapse images of the retracting edge of a HUVEC expressing tensin–GFP (pseudo-coloured red) and stained with a fluorescent membrane dye (pseudo-coloured green) at indicated times. Red arrowheads mark sites of FA disassembly, white arrowheads mark the trailing membrane retraction fibres. **b**, Total internal reflection fluorescence images of the retracting edge of a HUVEC stained for active INTβ1 (red), pERM (green) and phalloidin (blue). **c**, Time lapse confocal images of HUVEC expressing paxillin–GFP undergoing membrane retraction at indicated times 1 h after addition of DMSO (dimethyl sulfoxide, as vehicle control) or GNE-220. Arrows mark disassembling FAs. **d**, FA disassembly rates in HUVEC stably expressing paxillin–GFP and treated with the indicated agents. Each dot represents mean of an individual cell, >8 FA disassembly events per cell, representative of 3 experiments. **e**, Mean fluorescence intensity of cell-surface active INTβ1 (left) or ratio of active versus total INTβ1 (right) in CHO cells overexpressing talin-FERM–Cherry or moesin-FERM–Venus fusion proteins (+), or Cherry and/or Venus without the fused protein (−). Means of 3 experiments. **f**, Recombinant wild-type or mutant integrin β1ICD-coated beads were incubated with the indicated proteins. The pulled-down or input proteins were analysed by western blotting. An irrelevant protein RKIP served as negative control. IP, immunoprecipitation. **g**, Quantification of talin and moesin associated with β1ICD-coated beads in the presence of increasing concentrations of moesin. Means of three experiments. Scale bars, 5 μm.

also competed with moesin for binding to β1ICD (Extended Data Fig. 7i). These data suggest that moesin-FERM can inactivate INTβ1 by competing with talin for binding to β1ICD.

To understand why moesin-FERM cannot activate INTβ1, we compared INTβ1 activation in CHO cells expressing talin-FERM, moesin-FERM, or chimaeras of talin- and moesin-FERM. Replacing talin-F3 with moesin-F3 abolished INTβ1 activation, whereas replacing talin-F1F2 with moesin-F1F2 partially inhibited its activity (Extended Data Fig. 7j). Consistent with previous report[25], our data suggests that the talin-FERM subdomains support a unique conformation required for INTβ1 activation, which moesin lacks.

Anti–INTα5β1 antibodies restore membrane retraction

As *siMAP4K4* or *siMSN* impaired INTβ1 inactivation, we tested whether forced integrin–extracellular matrix detachment with a function-blocking antibody against human α5β1-integrin (anti-INTα5β1, Extended Data Fig. 8a) could reverse the knockdown phenotype in the HUVEC sprouting assay. Treatment with anti-INTα5β1 indeed restored the retraction deficit in *siMAP4K4*, *siMSN*, or GNE-220-treated cells (Fig. 6a).

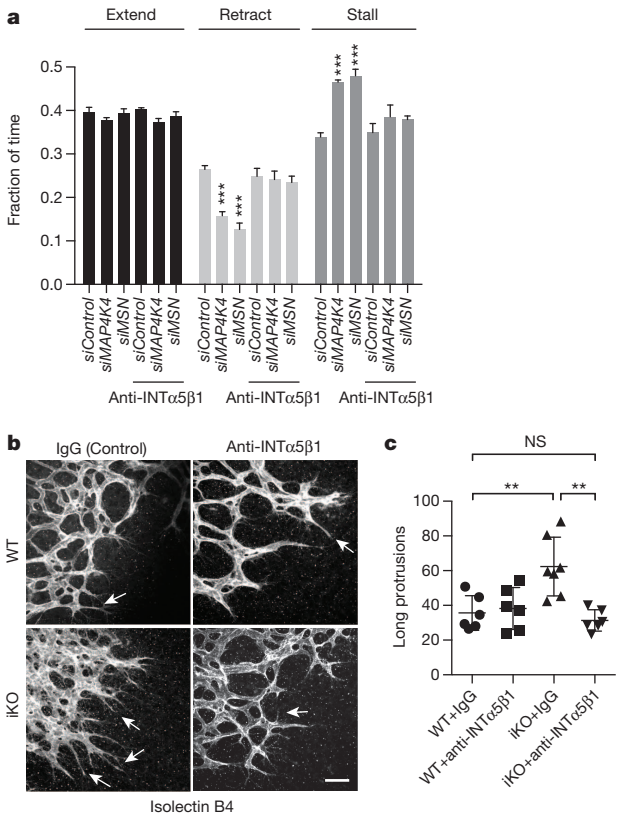

Figure 6 | Anti-INTα5β1 rescues *Map4k4* and *MSN* loss of function defects. **a**, Membrane dynamics in HUVEC sprouts from cells treated with the indicated reagents. Four beads per condition, >15 sprouts per bead were tracked over a 12-h period, representative of 3 experiments. **b**, Vascular front of P7 *Map4k4*$^{iKO/iKO}$ or wild-type retinas treated with a negative control antibody (IgG) or anti-murine-INTα5β1 antibody and stained for isolectin-B4. Arrows indicate long subcellular protrusions. **c**, Numbers of long membrane protrusions (>40 μm) per centimetre of retinal vascular edges. Each dot represents a mouse, the entire circumference of each retina was quantified. Representative of 3 experiments, each experiment contains multiple litters of mice. Scale bar, 50 μm.

We then used a function-blocking antibody against murine α5β1-integrin (Extended Data Fig. 8b) to test whether it can rescue the *Map4k4*$^{iKO/iKO}$ vascular defects. Although anti-INTα5β1 had no obvious effect on the retinal vessels in control mice, it reduced long membrane protrusions in *Map4k4*$^{iKO/iKO}$ mice, whereas a control antibody (IgG) did not (Fig. 6b, c). Deletion of *Map4k4* exon 6 in iKO pups was confirmed (Extended Data Fig. 8c).

These data support the hypothesis that MAP4K4 and moesin reduce talin–INTβ1 binding to inactivate INTβ1 and enable membrane retraction during endothelial cell migration (Extended Data Fig. 8d).

MAP4K4 regulates pathologic angiogenesis

Since angiogenesis contributes to human diseases, we evaluated the role of MAP4K4 in mouse models of cancer and eye disease. To inhibit MAP4K4 *in vivo*, we developed another MAP4K4 inhibitor, GNE-495, with good pharmacokinetic properties (Supplementary Table 1) because GNE-220 is rapidly cleared in rodents. GNE-495 was comparable to GNE-220 in each of the aforementioned cell-based assays (Extended Data Fig. 8e–g).

Implantation of *Map4k4*-wild-type tumour cells into *Map4k4*$^{iKO/iKO}$ mice revealed that loss of *Map4k4* in host tissues reduced tumour growth rate, tumour vascular perfusion, and endothelial cell membrane retraction (Extended Data Fig. 9a–g). In the oxygen-induced retinopathy model, GNE-495 reduced retinal neovascularization, vascular regrowth, and haemorrhage (Extended Data Fig. 9h–l). These data suggest that MAP4K4 regulates both normal and pathological angiogenesis.

Discussion

Cell migration requires assembly and disassembly of FAs. A number of mechanisms have been reported to regulate FA disassembly, including integrin internalization, degradation or inhibition of accessary proteins[26–28]. Here we identify a molecular cascade that promotes FA disassembly and highlight the importance of membrane retraction during angiogenesis.

Although our work focused on MAP4K4 in endothelial cells, published data suggest that MAP4K4 has a conserved role in regulating membrane dynamics across several species and cell types. In *Caenorhabditis elegans*, loss of the MAP4K4 homologue *mig-15* reduced axon branches in an ERM-dependent manner[29]. In *Drosophila*, the MAP4K4 homologue *msn* regulates epithelial cell migration during oocyte development by decreasing INTβ1 at the basal cell surface[30]. Together, these data demonstrate that MAP4K4 and its homologues have a conserved function in regulating membrane dynamics.

Note added in proof: Recently it was reported that MAP4K4 regulates focal adhesion disassembly in skin cells, indicating a conserved function of MAP4K4 in multiple cell types[31].

Online Content Methods, along with any additional Extended Data display items and Source Data, are available in the online version of the paper; references unique to these sections appear only in the online paper.

Received 6 December 2013; accepted 11 February 2015.
Published online 18 March 2015.

1. Ridley, A. *et al.* Cell migration: integrating signals from front to back. *Science* **302,** 1704–1709 (2003).
2. Hynes, R. O. Integrins: bidirectional, allosteric signaling machines. *Cell* **110,** 673–687 (2002).
3. Calderwood, D. A., Campbell, I. D. & Critchley, D. R. Talins and kindlins: partners in integrin-mediated adhesion. *Nature Rev. Mol. Cell Biol.* **14,** 503–517 10.1038/nrm3624 (2013).
4. Gardel, M. L., Schneider, I. C., Aratyn-Schaus, Y. & Waterman, C. M. Mechanical integration of actin and adhesion dynamics in cell migration. *Annu. Rev. Cell Dev. Biol.* **26,** 315–333 (2010).
5. Dan, I., Watanabe, N. M. & Kusumi, A. The Ste20 group kinases as regulators of MAP kinase cascades. *Trends Cell Biol.* **11,** 220–230 (2001).
6. Su, Y. C., Treisman, J. E. & Skolnik, E. Y. The *Drosophila* Ste20-related kinase misshapen is required for embryonic dorsal closure and acts through a JNK MAPK module on an evolutionarily conserved signaling pathway. *Genes Dev.* **12,** 2371–2380 (1998).
7. Xue, Y. *et al.* Mesodermal patterning defect in mice lacking the Ste20 NCK interacting kinase (NIK). *Development* **128,** 1559–1572 (2001).
8. Aouadi, M. *et al.* Orally delivered siRNA targeting macrophage Map4k4 suppresses systemic inflammation. *Nature* **458,** 1180–1184 (2009).
9. Kaneko, S. *et al.* Smad inhibition by the Ste20 kinase Misshapen. *Proc. Natl Acad. Sci. USA* **108,** 11127–11132 (2011).
10. Guntur, K. V., Guilherme, A., Xue, L., Chawla, A. & Czech, M. P. Map4k4 negatively regulates peroxisome proliferator-activated receptor (PPAR) gamma protein translation by suppressing the mammalian target of rapamycin (mTOR) signaling pathway in cultured adipocytes. *J. Biol. Chem.* **285,** 6595–6603 (2010).
11. Becker, E. *et al.* Nck-interacting Ste20 kinase couples Eph receptors to c-Jun N-terminal kinase and integrin activation. *Mol. Cell. Biol.* **20,** 1537–1545 (2000).
12. Baumgartner, M. *et al.* The Nck-interacting kinase phosphorylates ERM proteins for formation of lamellipodium by growth factors. *Proc. Natl Acad. Sci. USA* **103,** 13391–13396 (2006).
13. Lewellyn, L., Cetera, M. & Horne-Badovinac, S. Misshapen decreases integrin levels to promote epithelial motility and planar polarity in *Drosophila*. *J. Cell Biol.* **200,** 721–729 (2013).
14. Poinat, P. *et al.* A conserved interaction between β1 integrin/PAT-3 and Nck-interacting kinase/MIG-15 that mediates commissural axon navigation in *C. elegans*. *Curr. Biol.* **12,** 622–631 (2002).
15. Fehon, R. G., McClatchey, A. I. & Bretscher, A. Organizing the cell cortex: the role of ERM proteins. *Nature Rev. Mol. Cell Biol.* **11,** 276–287 (2010).
16. Lee, J. H. *et al.* Roles of p-ERM and Rho-ROCK signaling in lymphocyte polarity and uropod formation. *J. Cell Biol.* **167,** 327–337 (2004).
17. Gatto, C. L., Walker, B. J. & Lambert, S. Asymmetric ERM activation at the Schwann cell process tip is required in axon-associated motility. *J. Cell. Physiol.* **210,** 122–132 (2007).
18. Ridgway, J. *et al.* Inhibition of Dll4 signalling inhibits tumour growth by deregulating angiogenesis. *Nature* **444,** 1083–1087 (2006).
19. Dorrell, M. I. & Friedlander, M. Mechanisms of endothelial cell guidance and vascular patterning in the developing mouse retina. *Prog. Retin. Eye Res.* **25,** 277–295 (2006).

20. Berryman, M., Franck, Z. & Bretscher, A. Ezrin is concentrated in the apical microvilli of a wide variety of epithelial cells whereas moesin is found primarily in endothelial cells. *J. Cell Sci.* **105,** 1025–1043 (1993).
21. Carlson, T. R., Hu, H., Braren, R., Kim, Y. H. & Wang, R. A. Cell-autonomous requirement for beta1 integrin in endothelial cell adhesion, migration and survival during angiogenesis in mice. *Development* **135,** 2193–2202 (2008).
22. Zovein, A. C. *et al.* Beta1 integrin establishes endothelial cell polarity and arteriolar lumen formation via a Par3-dependent mechanism. *Dev. Cell* **18,** 39–51 (2010).
23. Harunaga, J. S. & Yamada, K. M. Cell-matrix adhesions in 3D. *Matrix Biol.* **30,** 363–368 (2011).
24. Amieva, M. R. & Furthmayr, H. Subcellular localization of moesin in dynamic filopodia, retraction fibers, and other structures involved in substrate exploration, attachment, and cell-cell contacts. *Exp. Cell Res.* **219,** 180–196 (1995).
25. Elliott, P. R. *et al.* The Structure of the talin head reveals a novel extended conformation of the FERM domain. *Structure* **18,** 1289–1299 (2010).
26. Bridgewater, R. E., Norman, J. C. & Caswell, P. T. Integrin trafficking at a glance. *J. Cell Sci.* **125,** 3695–3701 (2012).
27. Bhatt, A., Kaverina, I., Otey, C. & Huttenlocher, A. Regulation of focal complex composition and disassembly by the calcium-dependent protease calpain. *J. Cell Sci.* **115,** 3415–3425 (2002).
28. Bouvard, D., Pouwels, J., De Franceschi, N. & Ivaska, J. Integrin inactivators: balancing cellular functions *in vitro* and *in vivo*. *Nature Rev. Mol. Cell Biol.* **14,** 430–442 (2013).
29. Teulière, J., Gally, C., Garriga, G., Labouesse, M. & Georges-Labouesse, E. MIG-15 and ERM-1 promote growth cone directional migration in parallel to UNC-116 and WVE-1. *Development* **138,** 4475–4485 (2011).
30. Lewellyn, L., Cetera, M. & Horne-Badovinac, S. Misshapen decreases integrin levels to promote epithelial motility and planar polarity in *Drosophila*. *J. Cell Biol.* **200,** 721–729 (2013).
31. Yue, J. *et al.* Microtubules regulate focal adhesion dynamics through MAP4K4. *Dev. Cell* **31,** 572–585 (2014).

Supplementary Information is available in the online version of the paper.

Acknowledgements We thank L. Parker, R. Tam, K. Lyle, and B. Haley for contributing DNA constructs and siRNA design; H. Lu for initiating the chemical screen; J. Sudhamsu, P. Hass, J. Payandeh, and P. Lupardus for assisting with construct design and protein purification; J. Nonomiya, P. Wu, J. Wu, M. Lorenzo, H. Li, S. Schmidt for assay optimization, R. Ybarra and L. Magee for animal husbandry; S. Warming and M. Roose-Girma for generating floxed *Map4k4* mice; J. Boggs, T. Crawford, L. Wang, J. Drobnick and L. Gazzard for compound synthesis and pharmacokinetics studies; M. Sagolla for input on image acquisition and analyses; L. dePalatis, C. Reed for antibody generation, V. Pham, D. Kirkpatrick for kinase substrate screen, L. Murray, J. Burton and C. Wilson for discussions. H. Gerhardt for advice.

Author Contributions P.V. and W.Y. conceived the concept of the paper, designed most experiments, and co-wrote the paper. P.V. carried out the majority of the experiments. S.Y., E.M., S.G. carried out and supervised many *in vivo* studies. J.B., T.S., K.W. carried out several *in vitro* studies. S.F.H. carried out structural analysis of MAP4K4. C.N. is responsible for all experiments related to the generation and characterization of chemical inhibitors. A.C. and J.E.-A. wrote automated image analysis code and did some of the image data analyses. All authors contributed to the writing and proof-reading of the manuscript.

Author Information Reprints and permissions information is available at www.nature.com/reprints. The authors declare competing financial interests: details are available in the online version of the paper. Readers are welcome to comment on the online version of the paper. Correspondence and requests for materials should be addressed to W.Y. (loni@gene.com).

METHODS

***In vivo* studies.** All animals were handled according to guidelines from the Institutional Animal Care and Use Committee (IACUC) at Genentech, Inc.

The floxed *Map4k4* allele was generated using standard homologous recombination techniques. *Map4k4*$^{fl/fl}$ mice were crossed to Tie2-Cre mice[32] to generate conditional knockout (CKO) in the endothelium, or to Rosa26-CreERT2[33] mice to generate inducible knockout (iKO) in all tissues upon Tamoxifen induction. All mice used are in the C57BL/6N genetic background. For CKOs, timed pregnancies were set up between *Map4k4*$^{fl/+}$ and *Map4k4*$^{fl/+}$::Tie2-Cre parents, and E9.5-E18.5 embryos were analysed with plug date defined as E0.5. For iKOs, P1 pups with genotype of *Map4k4*$^{fl/fl}$ or *Map4k4*$^{fl/fl}$::Rosa26-CreERT2 were injected intraperitoneally daily with 80 mg per kg (body weight) tamoxifen dissolved in sunflower oil for 3 days, and P7 pups were analysed. For integrin rescue experiments, P1 pups were injected intraperitoneally daily with 80 mg per kg (body weight) Tamoxifen at 9 am, and 30 mg per kg (body weight) control antibody or anti-α5β1 antibody at 5 pm for 3 days. Antibody injection continued for three additional days.

Oxygen-induced retinopathy (OIR) model[34] was used to mimics vascular pathologies in human proliferative diabetic retinopathy and retinopathy of prematurity. Wild-type C57BL/6 pups were raised in 75% oxygen from P7 to P12, then returned to room air with daily intraperitoneally dosing of 100 mg per kg (body weight) MAP4K4 inhibitor GNE-495 or vehicle for 5 days. P17 pups were analysed. Pups from each litter were divided into the control and treatment groups based on body weights to ensure similar body weight distribution between groups.

For tumour studies, animals were injected with 80 mg per kg (body weight) tamoxifen intraperitoneally, once daily for 5 days to induce *Map4k4* deletion. Two weeks later, male mice with the ages between 6 and 12 weeks were grouped based on body weight and genotype to ensure equal body weight distribution. Mice were inoculated subcutaneously on the right lateral flank with 10^6 KPP-1 cells in 100 µl HBSS/Matrigel or 0.5 million TC-1 cells in 100 µl HBSS/Matrigel. Tumours were measured twice a week until they reached IACUC specified limits. For histology analysis, tumours were harvested 2 weeks later when they reached 200–500 mm^3. For tumour perfusion experiments, tail vein injections of 100 µl of a 1 mg ml^{-1} solution of fluorescein-labelled lycopersicon esculentum (Vector FL-1171) were performed 5 min before tissue harvest.

During the in-life portion of the animal studies, investigators were not blinded with regard to the genotypes and treatments.

Cell culture. HUVEC (Lonza, CC-2519) were cultured in complete EGM-2 (Lonza, CC-3156 and CC-4176). siRNA and plasmid transfections were performed with DharmaFECT1 (Dharmacon) and Targefect (TargetingSystems), respectively. HUVEC were assayed 3 days after siRNA transfection. CHO cells (ATCC, CCL-61) were cultured in DMEM supplemented with 10% FBS, 1 mM glutamate, and penicillin/streptomycin and transfected using Lipofectamine LTX (Life Technologies). Cells were tested at Genentech to ensure mycoplasma-negative.

HUVEC assays. HUVEC sprouting assays were performed as previously described[35]. For siRNA treatment, HUVEC were transfected 1 day before coating to beads. For chemical inhibitor treatment, inhibitor was added to media after fibrin was clotted. For immunofluorescence staining, beads were seeded in thin 100 µl fibrin clots. For scratch wound healing assay, HUVEC were transfected 2 days before re-seeding into a glass-bottom 96-wells plate. Wound area was measured using the Incucyte instrument (Essen BioScience). Permeability assays were performed as described previously[36]. For moesin rescue, an siRNA oligo targeting the UTR region of moesin was transfected into cells. Two days later, cells were transfected with cDNA contructs expressing moesin–GFP or moesin(T558A)–GFP and plated into a glass-bottom 96-wells plate. After overnight incubation, cells were fixed and stained.

For Dll4 inhibition, a previously characterized function-blocking antibody was added to media before fibrin clotting to ensure immediate delivery[37].

Constructs and virus production. *MAP4K4* was cloned by PCR from a cDNA library prepared from HUVEC. Point mutants were introduced by site directed mutagenesis. For expression, *MAP4K4* or *Lck-RFP* was cloned into pGIPz lentiviral vector, which were co-transfected with pCMVΔ8.9 and pVSV-G in HEK293T cells to generate viral particles. HUVEC were infected at 1–5 multiplicity of infection per cell and selected with 200 µg ml^{-1} hygromycin for 3 days. Tensin–GFP and moesin constructs were obtained from Origene. Moesin (M1-P297) and talin (M1-Q435) FERM domains were synthesized (Blue Heron) and inserted into expression vectors pDEST47 and pmCherry-C1 (AddGene, 632524) with N-terminal Venus or mCherry fusion, respectively. For the experiment shown in Extended Data Fig. 7f, Band4.1 FERM domain (S215–R488) and moesin FERM domain (M1–P297) were cloned into mCherry vector, and talin FERM domain (M1–Q435) in the Venus vector. For FERM chimaeras, the F2-F3 boundary was defined as Gly 230 for talin and Gly 202 for moesin. Inserts were synthesized and cloned into pmCherry-C1.

Histology. Mouse embryos, neonatal eyes with opening in the cornea, or bisected tumours were fixed overnight (embryos and tumours) or 1 h (eyes) at 4 °C. The crown of the skull was harvested and the outermost skin layer removed. Retinas were isolated and other eye tissues discarded. Tumours were bisected at midline and cryoprotected in 30% sucrose overnight and embedded in Optimal Cutting Temperature Compound OCT (Tissue Tek, 4583), and sectioned at 12 µm and 80 µm using a Cryostat (Leica model CM3050S). Tissue was permeabilized in 0.5% Triton X-100/0.05% Tween-20/10% goat serum/PBS. Primary antibodies, including anti-CD31 (BD Biosciences, 550274) and anti-VECadherin (BD Biosciences, 555289 for cell, R&D AF1002 for mouse embryos), anti-ERG (Santa Cruz, sc-353), and anti-isolectin-B4 (Sigma, L2140-1MG) were incubated overnight. Flattened whole-mount tissues or tumour sections were mounted with Fluoromount-G (Southern-Biotech 0100-01).

HUVEC cultured on glass-bottom chamber slides or in fibrin clots were fixed with 4% paraformaldehyde/PBS for 10 min before permeabilization in 0.1% Triton X-100/PBS and block in 10% goat serum/PBS. Cells were stained with antibodies against pERM (CST, 3149S), active INTβ1 (12G10, Millipore, MAB2247-1; or 9EG7, BD Biosciences, 550531), phalloidin (Invitrogen, A12379), INTαVβ5 (Millipore, MAB2019Z, and MAB1961) INTβ3 (Millipore, MAB1974 and CBL479), paxillin (Epitomics, 1500-1), or total INTβ1 (R&D Systems, MAB1778). Cells were analysed with confocal, epifluorescent, or TIRF microscopy as specified in the figure legends. Integrin β3 and αVβ5 were used to mark nascent adhesions[38]. Although moesin played a dominant role in endothelial cells, we were unable to identify a specific antibody against phospho-moesin, and had to use a phospho-ERM antibody.

***In vitro* kinase assays.** His-tagged MAP4K4 kinase domain (A2-E328) was expressed and purified from SF9 insect cells using standard procedures. 3 µg of purified kinase containing a T181E activating mutation was incubated with 100 µM moesin peptide LGRDKYKTLRQIRQ (Genentech) or purified Myc–Flag–moesin (Origene, TP305674) in 50 mM HEPES pH 7.2/10 mM $MgCl_2$/1 mM EGTA/0.01% Triton X-100 for 45 min at room temperature in the presence or absence of 3 µM ATP. Remaining ATP levels were assayed using KinaseGlo (Promega).

FACS. FACS analysis of activated β1-integrin was performed as previously described[39]. Fibronectin III(8-10) peptide (KeraFast, EUR108) was biotinylated with SS-Biotin (Pierce, 21441). Analysis was run on LSR Fortessa Cell Analyzer (BD). Cells expressing mCherry, Venus, or Cherry-tagged and Venus-tagged fusion proteins were gated by FACS based on Cherry or Venus signal intensity to make sure that equal levels of expression were compared between samples and across experiments. For the Band4.1 and moesin FERM domains comparison experiment, integrin activation levels for cherry positive cells were normalized to Cherry negative cells in the same sample. In the experiment reported in Extended Data Fig. 7j, lower level of Cherry signal was chosen for reasons explained in the legend of the Extended Data.

Competitive binding to β1ICD. His–Flag–β1ICD-coated beads were prepared as described[40]. His–Flag-tagged wild-type and mutant (Y783A/Y795A) β1ICD[41] were purified from bacterial lysates using nickel beads (Sigma, H9914) followed by a size exclusion column. To remove aggregates, β1ICD was denatured with 8 M urea, and 1 mg of protein was loaded onto 50 µl of magnetic beads. After 1 h incubation, beads were renatured with decreasing urea concentrations and resuspended in 500 µl buffer XT (50 mM NaCl/150 mM sucrose/10 mM PIPES/3 mM $MgCl_2$/0.05%Ttriton/protease/ phosphatase inhibitor cocktail). Flag–talin-FERM and Flag–moesin-FERM were bacterially expressed and purified using anti-Flag beads. Both were eluted with 3× Flag peptide (Sigma). The negative control protein RKIP (Raf kinase inhibitor protein) was expressed and purified following similar protocol.

Image data acquisition and analysis. Investigators who carried out the automated image data analysis were blinded with regard to genotype and treatment at the step when individual images were segmented and quantified.

For membrane length detection, HUVEC coated beads were fixed and stained with phalloidin and DAPI to outline cells and nuclei, respectively. Compressed *z*-stack images from 4× epifluorescence scanning (ImageXpress Micro) were analysed with the MetaXpress Neurite detect algorithm. The sum of lengths from all protrusive structures was scored for each bead. This analysis does not distinguish between sub-cellular protrusions versus sprouts. Data presented in Figs 1a–c, 3a, b and Extended Figs 1b and 7a.

For live imaging of fluorescent HUVEC in sprouting assay, cells stably infected with lentiviral vectors were coated on beads and allowed to sprout for 2 days. Hoescht33342 was added atop the fibrin overnight. Fibrin clots were placed on 3i Inverted Marianas microscope with live cell chamber and imaged every 10 min at 20× for 16 h. Measurements were also carried out within the first 12 h of sprouting using unstained cultures imaged at 10× every 10 min. Subcellular membrane protrusion, retraction, and stalling were tracked manually in SlideBook. Sprouts consisting of cell bodies were excluded from this analysis. Protrusion and retraction were defined as membrane movements greater than 4 µm away from or towards the bead per 10 min interval, stalling was defined as movement less than 4 µm in either direction, branching was defined as bifurcating protrusions greater than 5 µm over a 16 h period. Data presented in Figs 1d–g, 3c, 6a.

For elongated FA measurement, transfected or inhibitor treated cells were placed on Leica spinning disk confocal and imaged at 40× every 3 min for ~ 8 h. Cells were stained with Far Red Membrane Tracker (Life Technologies, C34552) and transfected with tensin–GFP or infected with adenovirus expressing paxillin–GFP, or were stained with DAPI, antibody against activated β1-integrin, and phalloidin. For FA disassembly analysis, FA in retracting membranes were tracked to determine the rate of movement. For long FA decay time and FA assembly rate analysis, movies were uploaded to Focal Adhesion Analysis Server[42]. For FA decay time analysis, the first time point were chosen when a FA reached its longest length and was tracked for analysis. For assembly rates, adhesion tracks with a P value less than 0.05, R-squared greater than 0.7, and minimum slope of 0.01 were analysed. For elongated adhesion analysis, nuclei were segmented and counted using a top-hat filter followed by adaptive intensity threshold. Actin and adhesion stains were then segmented using a combination of adaptive and local intensity thresholds. Cell objects were created by a logical OR combination of adhesion and actin masks and were required to contain nuclear staining. Adhesions were further classified as puncta ($<2\ \mu m^2$), focal adhesions, or long focal adhesions (long FAs) defined as long and thin (eccentricity >5), with strong intensity (>1.5 times the mean of the intensity of all adhesions), and with minimal branching (solidity >0.3).

For quantification of pERM spikes: DAPI, phalloidin, and pERM images were segmented using both local and adaptive intensity thresholds. Cell objects were defined as regions that contained either actin or pERM staining and also contained a nuclear object. The cell body was selected by a morphological opening with kernel size of 10 μm to remove any protrusive structures. Protrusions were then identified as non-cell-body cellular structures of significant pERM intensity with area greater than 30 μm^2 and less than 650 μm^2. The number of pERM-positive protrusions per cell was calculated by dividing the number of protrusions per field of view by the number of nuclear objects in the same field.

For long membrane protrusions along the migration front of the embryonic head skin and the neonatal retinal vasculature: vascular stain from whole-mounted embryonic head skins or neonatal retinas was segmented with both local and adaptive intensity thresholds. To identify subcellular membrane protrusions along the migration front, gaps within the vascular network were filled to obtain a distinct edge, and thin membrane protrusions along the edge were identified by a morphological opening with kernel size of 15 μm. This diameter is too thin to contain a nucleus and, therefore, distinguishes subcellular structures. These structures were then further classified as subcellular protrusions if they were long and thin (eccentricity >2), had significant intensity (>mean intensity of the vascular stain), and had a length exceeding 40 μm. The eccentricity and length criteria were chosen because protrusions of this phenotype were rare in wild-type animals (data not shown). The length of the vascular edge was estimated by a flattened perimeter obtained by a series of morphological openings and closings with a maximum kernel of size 400 μm. The number of long subcellular membrane protrusions was counted and normalized by the length of the flattened vascular edge perimeter. The entire perimeter of a retina from each animal was quantified.

For pathologic vessel formation in the OIR model: 3D images of whole-mounted retinas from the OIR model were segmented for very bright (>3× the average vascular intensity in that plane) or moderately bright and large regions (>6,000 μm^2 in a single plane). Normal vasculature was excluded by removing objects with aspect ratio greater than 4. All images were manually inspected to add missing segments or remove false positives. Pathological vascular coverage was then quantified as the ratio between total pathological vessel area and total retinal area.

For tumour vascular perfusion: entire sections of each tumour were scanned at 20× using the automated Tissuegnostic scanning system (http://www.tissuegnostics.com/). Viable tumour areas were identified by nuclei morphology based on DAPI staining. Total $CD31^+$ vascular areas were measured. Within the $CD31^+$ areas, $FITC^+$ areas were then measured and calculated as ratios to the total $CD31^+$ areas. These ratios are used to evaluate functionality of the tumour vasculature.

For tumour vascular patterning: tumour vasculatures were imaged by confocal microscopy at 40× magnification. Since areas at the border between tumour and overlying skin contain many sprouts, we focused our analysis in this region. Five tumours from each genotype, and 5–6 images per tumour were analysed. Lengths of membrane protrusion from each sprout are labelled and measured manually. A total of 85 membrane protrusions from the control tumours, and 84 protrusions from the Map4k4 iKO tumours were quantified. Results are expressed at percent of membrane protrusions greater than 40 μm per tumour.

For VE-Cadherin analysis, 80× confocal images were used to generate 10 μm junctional segments. Each segment was then scored as being inhibited (straight, linear junction), mixed (finger-like projections), or active (honeycomb or serrated), modelled on previous analyses[43]. The "active" junction refers to diffused or serrated junction that reflects junctional remodelling, the "inhibited" morphology refers to linear junctions that reflect relative junctional stability, and the "mixed" junction contains both morphologies within the defined length. The number of each segment type was scored as fraction of total segments in that image.

Image data were analysed using automated methods developed using customized Matlab codes in our group. All computer codes are deposited at the following site: (https://github.com/ailey/Vitorino_Nature_2015).

For all studies we did not exclude samples from analysis except Extended Data Fig. 9c, d. Six tissue sections were excluded in this study because they failed to show CD31 staining in large portion of the tumours, indicating technical failure. These sections were excluded from the analysis.

Statistical analysis. For all figures, statistical analyses were carried out using GraphPad Prism (http://www.graphpad.com/). The majority of data sets with sufficient n numbers to run the D'Agnostino & Pearson Omnibus normality test met the criteria for a normal distribution, therefore these data were analysed using unpaired Student's t-test. For data that did not pass the normal distribution test, Mann–Whitney test was used. For data sets that the n numbers were too small for D'Agnostino & Pearson Omnibus normality test, we assumed normal distribution based on the appearance of the data.

For all tests, variance similarity was determined using the Prism program. When variances were significantly different between comparators, Welch's correction was applied.

In all figures, statistical significance between the indicated sample and control or between marked pairs are designated: $*P < 0.05$, $**P < 0.01$, $***P < 0.001$, or NS ($P > 0.05$).

Endothelial cell isolation from E15.5 embryos and determination of *Map4k4* exon 6 expression. E15.5 embryos were harvested and dissociated into a single cell suspension using a combination of both enzymatic digestion with 1 μg ml^{-1} of collagenase D (Roche, 11088866001) and gentle agitation with a gentleMACS Dissociator (Miltenyi Biotec). Cell suspension was incubated with anti-CD31 (BD Biosciences) conjugated Dynabeads (Invitrogen, 110.35), anti-CD31 was incubated with beads the night before), and separated into endothelial cells (those bound to beads) and non-endothelial cell (unbound cells). Total RNA was isolated using a RNeasy Mini Kit (Qiagen, 74134). cDNA was synthesized using a High Capacity cDNA Reverse Transcription Kit (Applied Biosystems, 4368814). Quantitative PCR on triplicate samples per condition was carried out using 50ng of cDNA in a ViiA7 machine (Applied Biosystems) using the Comparative CT program. *Map4k4* expression was determined relative to housekeeping gene *RPS13*. Primer/probe information is listed below. The *Map4k4* primers amplify sequences spanning exons 6 and 7. Endothelial cell purity was assessed by relative expression of VECadherin to housekeeping gene *RPS13*.

Mouse *Map4k4* primer/probe information. *Map4k4* Primer/Probe set: Applied Biosystems Mm00500800_mH, VECadherin Primer/Probe set: Applied Biosystems Mm00486938_m1,RPS13 probe and primers: 5′-CGGGTGCTCCCACCTAATTGGA-3′-FAM dye (probe), 5′-CACCGATTGGCTCGATACTA-3′ (forward primer) and 5′-TAGAGCAGAGGCTGTGGATG-3′ (reverse primer). Synthesized at Genentech.

Endothelial cell proliferation studies. For bead sprouting assays, 10 μM EdU (5-ethylnyl-2′-deoxyuridine) was added on day 3 of sprouting. Cells were fixed 16 h later. For head skin analysis, pregnant female mice were injected with 2 mg of EdU 4 h before embryo harvest. For retinal analysis, pups were injected with 50 mg per kg EdU on P6 before retinal harvest on P7. For all experiments, EdU was stained using Click-iT Imaging Kit from Invitrogen.

siRNA oligo sequences. *MAP4K4* siRNA: (1) 5′-GACCAACUCUGGCUUGUUA-3′, (2) 5′-UAUAAGGGUCGACAUGUUA-3′, (3) 5′-AGAGCGACAGAGACATTTATT-3′. *MSN* siRNA: (1) 5′-CGUAUGCUGUCCAGUCUAA-3′, (2) 5′-UCGCAAGCCUGAUACCAUU-3′, (3) 5′-GAGGGAAGUUUGGUUCUUU-3′, (4) 5′-GGTCTAAAGTGAGCTCTATGG-3′ (UTR). ON-TARGETplus Non-Targeting pool (negative control for all siRNA experiments): (1) 5′-UGGUUUACAUGUCGACUAA-3′, (2) 5′-UGGUUUACAUGUUGUGUGA-3′, (3) 5′-UGGUUUACAUGUUUUCUGA-3′, (4) 5′-UGGUUUACAUGUUUUCCUA-3′.

Generation and characterization of anti-α5β1-integrin monoclonal antibodies (MAbs)

Anti-human-α5β1-integrin MAb. HUVEC were used to immunize Armenian hamsters and the immunized animals were subsequently boosted with recombinant human INTα5β1 extracellular domain (expressed and purified at Genentech). A monoclonal antibody (18C12) that specifically recognized the heterodimeric human α5β1 but not the α5 or β1 subunit alone or other integrins was identified by conventional hybridoma techniques. The affinity of 18C12 for human INTα5β1 was determined by Scatchard analysis against HUVEC that expresses the murine antigen, the affinity is $K_D = 0.06$ nM.

The ability of the anti-human α5β1 MAB 18C12 to inhibit INTα5β1 function was assessed for its ability to inhibit the migration of HUVEC in a Boyden Chamber assay described below. HTS multiwell plates (24-wells with pore size 8 μm from Becton, Dickinson and Company) were coated with 1 μg ml^{-1} fibronectin in 0.05 M

sodium carbonate buffer (pH 9.6) at 4 °C overnight. After washing with phosphate-buffered saline (PBS), 500 µl of EGM-2 medium (Lonza, CC-3162) with 0.1% bovine serum albumin (Sigma-Aldrich, A1933) was added to the bottom well. 50,000 HUVEC in 100 µl EGM-2 with 0.1% BSA were added to the top well and allowed to attached for 1 h. A human IgG1 control antibody at 10 µg ml^{-1} (anti-gD, Genentech Inc.) and serial dilutions of 18C12 were added to the top well at the concentrations indicated in Extended Data Fig. 6a. To stimulate migration, 20 ng ml^{-1} of VEGF-A (R&D Systems, 293-VE) was added to the bottom chamber of each well after 15 min of incubation with the respective antibodies. The plates were then incubated for 6 h. Cells that did not migrate were scraped off the upper chamber with a sponge swab, washed with PBS and scraped again. Cells that migrated through the membrane to the bottom chamber were fixed with 500 µl methanol for 5 min and stained with 500 µl Sytox green (Molecular Probes) for at least 20 min or overnight while protected from light. Pictures of each well were taken using a 5× objective on an AxioVision AC camera (Carl Zeiss MicroImaging GmbH). NIH Image J software was used to count the migrated cells and PRISM (GraphPad Software) was used to present the results.

Anti-murine-α5β1-integrin MAb. Murine INTα5β1 protein was purified from frozen mouse uterus (Pel-Freeze Biologicals), which were homogenized in water + 0.5 mM phenylmethanesulphonylfluoride (PMSF) at 4 °C and centrifuged. The supernatant was discarded and membrane proteins were extracted from the pellet by stirring for 1 h at room temperature in 20 mM Tris pH 8, 1 mM EGTA, and 0.5 mM PMSF, centrifuged and resuspended in 20 mM Tris pH 7.5, 0.6 M KCl and 0.5 mM PMSF. This was again centrifuged and the pellet was lysed overnight at 4 °C in 20 mM Tris pH 7.5, 0.5% Triton X-100, 1 mM $CaCl_2$, 1 mM $MgCl_2$, and 0.5 mM PMSF. The lysate was centrifuged and supernatant was loaded onto a prepared column of Affi-Gel resin (Bio-Rad Laboratories, 153-6047) coupled to a rat anti-mouse INTα5β1 antibody (BD Pharmingen, clone 5H10). The column was washed with 20 mM Tris pH 7.5, 1 mM $CaCl_2$, 1 mM $MgCl_2$, 0.2 M NaCl and eluted with 50 mM sodium citrate pH 4, 0.1% Triton X-100. The presence of both α and β subunits in the purified sample was confirmed by mass spectrometry.

The purified murine INTα5β1 was subsequently used to immunize and boost Armenian hamsters. A monoclonal antibody (10E7) that specifically recognized the heterodimeric murine α5β1 but that also did not recognize either the α5 or β1 subunit alone or other integrins was identified by conventional hybridoma techniques. The affinity of 10E7 for murine INTα5β1 was determined by Scatchard analysis against murine endothelial cell line 2H11 (ATCC, CRL-2163) that expresses the murine antigen, the affinity is $K_D = 0.3$ nM.

The ability of the anti-murine α5β1 MAB 10E7 to inhibit INTα5β1 function was assessed for its ability to inhibit the migration of Chinese Hamster Ovary B2 cells[44] stably expressing murine α5β1 (CHOB2-mα5β1) on a fibronectin substrate in response to serum. Migration assay was carried out as described above with the following modifications: high glucose Dulbecco's modified Eagle medium was used instead of EGM-2, cells were stimulated to migrate by 1% fetal bovine serum (VWR, 97068-101) instead of VEGFA. A negative control hamster IgG antibody (anti-gD, Genentech Inc.) or serial dilutions of 10E7 were added in top wells at the concentrations indicated in Extended Data Fig. 6b before cells were stimulated to migrate.

Generation of MAP4K4 small molecule antagonists

General chemistry. All solvents and reagents were used as obtained. Reactions involving air or moisture sensitive reagents were carried out under nitrogen atmosphere. Microwave reactions were performed using CEM Discover and Biotage Initiator reactors. NMR spectra were recorded in a deuterated solvent with a Bruker Avance 300 or 400 MHz NMR spectrometer, and referenced to trimethylsilane (TMS). Chemical shifts are expressed as δ units using TMS as the external standard (in NMR description, s = singlet, d = doublet, *t* = triplet, q = quartet, m = multiplet, and br = broad peak). All coupling constants (*J*) are reported in Hertz. Mass spectra were measured with a Finnigan SSQ710C spectrometer using an ESI source coupled to a Waters 600MS HPLC system operating in reverse mode with an X-bridge phenyl column of dimensions 150 mm by 2.6 mm, with 5 µm-size particles. Analytical purity was >95% unless stated otherwise. The following analytical method was used to determine chemical purity of final compounds unless otherwise stated: HPLC-Agilent 1200, water with 0.05% trifluoroacetic acid (TFA), acetonitrile with 0.05% TFA, Agilent Zorbax SD-C18, 1.8 µM, 2.1 × 30 mm, 40 °C, 3–95% B in 8.5 min, 95% in 2.5 min, 400 µl min^{-1}, 220 nm and 254 nm, equipped with Agilent quadrupole 6140, ESI positive, 110–800 amu.

2-(3-Cyano-pyridin-2-ylamino)-acetamide. Glycinamide (8.8 g, 79.4 mmol) and sodium carbonate (4.6 g, 43.3 mmol) were suspended in DMSO (200 ml) and stirred at ambient temperature for 16 h. The solid was removed by filtration through Celite, the filtrate treated with 2-chloronicotinonitrile (10.0 g, 72.2 mmol) and potassium fluoride (10.0 g, 173.3 mmol) and heated at 120 °C for 4 h. The mixture was allowed to cool to ambient temperature then diluted with water (800 ml). The precipitated solid was collected by filtration, washed with dichloromethane (50 ml) and water (50 ml), then triturated with diethyl ether (100 ml), filtered and left to air dry which afforded the title compound as an off-white solid (6.7 g, 53%). ^{1}H NMR (400 MHz, DMSO-d_6) 8.26 (dd, J = 4.9 Hz, 1.8 Hz, 1H), 7.93 (dd, J = 7.6 Hz, 1.8 Hz, 1H), 7.40 (s, 1H), 7.12 (t, J = 4.9 Hz, 1H), 7.00 (s, 1H), 6.69 (dd, J = 7.6 Hz, 4.9 Hz, 1H), 3.34 (s, 2H).

2-(5-bromo-3-cyano-pyridin-2-ylamino)-acetamide. A solution of *N*-bromosuccinamide (7.1 g, 38.2 mmol) in *N,N*-dimethylformamide (20 ml) was added drop-wise over 25 min to a suspension of 2-(3-cyano-pyridin-2-ylamino)-acetamide (6.7 g, 38.3 mmol) in *N,N*-dimethylformamide (30 ml). On complete addition the mixture was allowed to stir at ambient temperature for 16 h then poured onto water (400 ml). The precipitated solid was collected by filtration, washed with water (50 ml) and left to air dry which gave the title compound as a white solid (8.35 g, 96%). ^{1}H NMR (300 MHz, DMSO-d_6) 8.35 (d, J = 2.5 Hz, 1H), 8.24 (d, J = 2.5 Hz, 1H), 7.36–7.44 (m, 2H), 7.01 (s, 1H), 3.85 (d, J = 5.6 Hz, 1H). LC/MS (ESI+): R_T = 2.23 min, *m/z*: 257 (M+H$^+$).

3-Amino-5-bromo-1*H*-pyrrolo[2,3-b]pyridine-2-carboxylic acid amide. A suspension of 2-(5-bromo-3-cyano-pyridin-2-ylamino)-acetamide (8.35 g, 32.7 mmol) and sodium hydrogen carbonate (5.5 g, 65.5 mmol) in ethanol (150 ml) was heated under reflux for 66 h. The mixture was allowed to cool to ambient temperature then cooled further in an ice/water bath. The precipitated solid was collected by filtration, washed with ethanol (15 ml), water (2 × 20 ml), ethanol (20 ml) and diethyl ether (20 ml) and left to air dry to afford the title compound as a yellow solid (5.9 g, 71%). ^{1}H NMR (300 MHz, DMSO-d_6) 8.38 (d, J = 2.3 Hz, 1H), 8.32 (d, J = 2.3 Hz, 1H), 7.19 (s, 2H), 5.82 (s, 2H). LC/MS (ESI+): R_T = 2.38 min, *m/z*: 257 (M+H$^+$).

5-Bromo-3-[(1-methyl-1*H*-pyrazole-4-carbonyl)-amino]-1*H*-pyrrolo[2,3-b] pyridine-2-carboxylic acid amide. A suspension of 3-amino-5-bromo-1*H*-pyrrolo [2,3-b]pyridine-2-carboxylic acid amide (5.9 g, 23.2 mmol) and 1-methyl-1*H*-pyrazole-4-carbonyl chloride (4.02 g, 27.8 mmol) in pyridine (350 ml) were heated at 80 °C for 18 h. The mixture was allowed to cool to ambient temperature then poured into water. The resultant precipitated solid was collected by filtration, washed with water and diethyl ether and dried at 60 °C under high vacuum pressure to afford the title compound (6.6 g, 78%). ^{1}H NMR (300 MHz, DMSO-d_6) 10.79 (s, 1H), 8.67 (d, J = 2.3 Hz, 1H), 8.46 (d, J = 2.3 Hz, 1H), 8.33 (d, J = 2.9 Hz, 2H), 7.93 (d, J = 0.8 Hz, 1H), 3.92 (s, 3H). LC/MS (ESI+): R_T = 2.54 min, *m/z*: 365 (M+H$^+$).

8-bromo-2-(1-methyl-1*H*-pyrazol-4-yl)-3,5-dihydro-4*H*-pyrido[3′,2′:4,5]pyrrolo [3,2-*d*]pyrimidin-4-one. A suspension of 5-bromo-3-[(1-methyl-1*H*-pyrazole-4-carbonyl)-amino]-1*H*-pyrrolo[2,3-b]pyridine-2-carboxylic acid amide (1.0 g, 2.74 mmol) in 10% w/w aqueous potassium hydroxide (8 ml) and ethanol (4 ml) was heated under microwave irradiation at 170 °C for 1 h. The mixture was allowed to cool to ambient temperature, diluted with water and the resultant precipitated solid was collected by filtration. The solid was washed sequentially with water, methanol:diethyl ether and diethyl ether and left to air dry. The remaining material was afforded as a white solid (762 mg, 80%). ^{1}H NMR (300 MHz, DMSO-d_6) 8.40-8.35 (m, 2H), 8.08 (s, 1H), 7.89 (s, 1H), 3.87 (s, 3H). LC/MS (ESI+): R_T = 6.98 min, *m/z*: 347 (M+H$^+$).

2-(1-methyl-1*H*-pyrazol-4-yl)-8-(4-(4-methylpiperazin-1-yl)phenyl)-3,5-dihydro-4*H*-pyrido[3′,2′:4,5]pyrrolo[3,2-*d*]pyrimidin-4-one. 8-bromo-2-(1-methyl-1*H*-pyrazol-4-yl)-3,5-dihydro-4*H*-pyrido[3′,2′:4,5]pyrrolo[3,2-*d*]pyrimidin-4-one (762 mg, 2.19 mmol) was dissolved in a mixture of 1,4-dioxane and DMSO and (4-(4-methylpiperazin-1-yl)phenyl)boronic acid was added at once followed by 1 M aqueous potassium acetate solution. To the mixture was added 1,1′-*bis*(diphenylphosphino)-ferrocene]dichloropalladium(II) (5 mol%) and the reaction mixture was heated with microwave irradiation at 100 °C for 1 h. The mixture was cooled to ambient temperature and filtered through a plug of Celite eluting with ethyl acetate. The filtrate was concentrated and the residue was purified by flash column chromatography (5–10% methanol/dichloromethane). The fractions containing the desired product were concentrated and dried under high vacuum pressure to yield 2-(1-methyl-1*H*-pyrazol-4-yl)-8-(4-(4-methylpiperazin-1-yl)phenyl)-3,5-dihydro-4*H*-pyrido[3′,2′:4,5]pyrrolo[3,2-*d*]pyrimidin-4-one (530 mg, 55%). ^{1}H NMR (300 MHz, DMSO-d_6) 12.55 (s, 2H), 8.81 (d, J = 2.3 Hz, 1H), 8.51–8.47 (m, 2H), 8.22 (s, 1H), 7.67 (d, J = 8.3 Hz, 2H), 7.07 (d, J = 8.3 Hz, 2H), 3.93 (s, 3H), 3.24–3.18 (m, 4H), 2.44–2.50 (m, 4H), 2.24 (s, 3H). LC/MS (ESI+): R_T = 5.05 min, *m/z*: 441 (M+H$^+$).

4-chloro-2-(1-methyl-1*H*-pyrazol-4-yl)-8-(4-(4-methylpiperazin-1-yl)phenyl)-5*H*-pyrido[3′,2′:4,5]pyrrolo[3,2-*d*]pyrimidine. 2-(1-methyl-1*H*-pyrazol-4-yl)-8-(4-(4-methylpiperazin-1-yl)phenyl)-3,5-dihydro-4*H*-pyrido[3′,2′:4,5]pyrrolo[3,2-*d*] pyrimidin-4-one (180 mg, 0.41 mmol) was suspended in neat $POCl_3$ under an inert atmosphere and heated under reflux for 12 h. The reaction mixture was allowed to cool to ambient temperature and evaporated. The resultant residue was treated with ice and the pH of the aqueous phase was adjusted to between 7 and 9 by the addition of saturated aqueous sodium hydrogen carbonate solution. The solid was collected by filtration, washed with water and diethyl ether and used crude in the next step.

4-methyl-2-(1-methyl-1*H*-pyrazol-4-yl)-8-(4-(4-methylpiperazin-1-yl)phenyl)-5*H*-pyrido[3′,2′:4,5]pyrrolo[3,2-*d*]pyrimidine (GNE-220). Tetramethyltin (0.023 ml, 0.168 mmol) was added to a degassed suspension of 4-chloro-2-(1-methyl-1*H*-pyrazol-4-yl)-8-(4-(4-methylpiperazin-1-yl)phenyl)-5*H*-pyrido[3′,2′:4,5]pyrrolo [3,2-*d*]pyrimidine (70 mg, 0.153 mmol), lithium chloride (19 mg, 0.458 mmol) and *bis*(triphenylphosphine)palladium(II) dichloride (11 mg, 0.015 mmol) in dimethylformamide (2 ml) and was heated under microwave irradiation at 140 °C for 20 min. The reaction mixture was diluted with water (10 ml), the precipitated solid was removed by filtration, then washed with water and diethyl ether. The filtrate was concentrated under reduced pressure and the resultant residue triturated with diethyl ether then methanol to give the title compound as a cream solid (29 mg, 43%). ^{1}H NMR (400 MHz, DMSO-d_6) δ 12.35 (s, 1H), 8.93 (d, J = 2.2 Hz, 1H), 8.68 (d, J = 2.2 Hz, 1H), 8.35 (s, 1H), 8.06 (s, 1H), 7.70 (d, J = 8.8 Hz, 2H), 7.07 (d, J = 8.8 Hz, 2H), 3.91 (s, 3H), 3.21 (t, J = 4.9 Hz, 4H), 2.79 (s, 3H), 2.47–2.45 (m, 4H), 2.23 (s, 3H). LC/MS (ESI+): R_T = 5.55 min m/z 439 ($M+H^+$).

5-Fluoro-2-(3-fluorophenyl)pyridine. After a mixture of 2-bromo-5-fluoropyridine (50 g, 0.284 mol), 3-fluorophenylboronic acid (48 g, 0.343 mol), Pd(dppf)Cl_2 (5.0 g, 6.8 mmol,) and K_2CO_3 (178.5 g, 0.568 mol) in dioxane/H_2O (500 ml/150 ml) was degassed 3 times, the mixture was heated to 80∼100 °C for 3 h under N_2. The mixture was filtered through diatomite, and dioxane was removed under reduced pressure. Ethyl acetate (1.0 l) was added, and the organic phase separated, concentrated, and purified by column chromatography (20:1∼10:1 petroleum ether:ethyl acetate) to give desired product (50 g, 92%). ^{1}H NMR (400 MHz, $CDCl_3$) δ 8.54 (s, 1H), 7.72–7.65 (m, 3H), 7.49–7.39 (m, 2H), 7.08 (m, 1H)

5-Fluoro-2-(3-fluorophenyl)pyridine 1-oxide. 5-Fluoro-2-(3-fluorophenyl) pyridine (50 g, 0.262 mol), *m*-CPBA (106 g, 0.523 mol, 2eq) in dichloromethane was heated at reflux for 16 h. After most of the starting material was consumed (as indicated by TLC), the mixture was cooled to room temperature, and a $Na_2S_2O_3$ solution was added slowly, until there was no peroxide left (KI starch paper). (Caution: peroxide may be explosive.). Dichloromethane was removed and the yellow precipitate was collected and washed with saturated $NaHCO_3$ solution, until 3-chlorobenzoic acid was completely removed. The crude compound was dried and was used in next step without further purification (45 g, 83%). ^{1}H NMR (400 MHz, $CDCl_3$) δ 8.23–8.25 (m, 1H), 7.53 (m, 1H), 7.49–7.36 (m, 3H), 7.16–7.09 (m, 2H).

3-Fluoro-6-(3-fluorophenyl)picolinonitrile. To a solution of 5-fluoro-2-(3-fluorophenyl)pyridine 1-oxide (38 g, 0.183 mol) in acetonitrile (400 ml) was added TMSCN (73 g, 0.734 mol) and Et_3N (93 g, 0.917 mol). After the mixture was heated at reflux for 12 h under N_2, it was concentrated and purified by column chromatography (20% ethyl acetate in petroleum ether) to give 3-fluoro-6-(3-fluorophenyl) picolinonitrile (20 g, 50%). ^{1}H NMR (DMSO-d_6 400 MHz) δ 8.47–8.44 (m, 1H), 8.21–8.19 (m, 1H), 7.91–7.83 (m, 2H), 7.56–7.54 (m, 1H), 7.34–7.29 (m, 1H).

Diethyl 2-(2-cyano-6-(3-fluorophenyl)pyridin-3-yl)malonate. To a stirred solution of NaH (11.15 g, 278.81 mmol, 60%) in tetrahydrofuran (100 ml) was added diethyl malonate (44.66 g, 278.81 mmol) in tetrahydrofuran (50 ml) drop-wise at 0 °C under N_2. After the reaction mixture was stirred at 0 °C for 10 min, 3-fluoro-6-(3-fluorophenyl)picolinonitrile (30 g, 138.8 mmol) in tetrahydrofuran (100 ml) was added. After the reaction mixture was heated at reflux for 4 h under N_2, it was extracted with ethyl acetate (500 ml ×2), washed with saturated NaCl (300 ml), dried over Na_2SO_4, and concentrated to give the crude title product, which was used for the next step directly (50 g, 100%).

Ethyl 2-(2-cyano-6-(3-fluorophenyl)pyridin-3-yl)acetate. To a solution of diethyl 2-(2-cyano-6-(3-fluorophenyl)pyridin-3-yl)malonate (50 g, 140.31 mmol) in DMSO (300 ml), was added H_2O (6 ml), LiCl (23.32 g, 550.02 mmol) and the mixture was stirred at 100 °C overnight. After cooling to room temperature, it was extracted with ethyl acetate (300 ml ×3), washed with sat NaCl (300 ml), dried over Na_2SO_4, concentrated and purified by column (petroleum ether:ethyl acetate = 8:1) to give the title product as white solid (20 g, 50% over two steps). ^{1}H NMR (400 MHz, DMSO-*d6*) δ 8.33 (d, J = 8.4 Hz, 1H), 8.11 (d, J = 8.4 Hz, 1H), 7.96–7.87 (m, 2 H), 7.59–7.54 (m, 1H), 7.36–7.31 (m, 1H), 4.16–4.10 (m, 2H), 4.02 (s, 2H), 1.19 (t, J = 7.0 Hz, 3H).

Ethyl 2-(2-cyano-6-(3-fluorophenyl)pyridin-3-yl)-3-(dimethylamino)acrylate. A solution of compound ethyl 2-(2-cyano-6-(3-fluorophenyl)pyridin-3-yl)acetate (50 g, 0.176 mol) and dimethylformamide-DMA (168 g, 1.41 mol) in dimethylformamide (200 ml) was heated at 80 °C overnight. The mixture was concentrated and purified by column chromatography to give the product (45 g, 75%). ^{1}H NMR (400 MHz, DMSO-*d6*) δ 8.24 (d, J = 8.4 Hz, 2H), 7.96 (d, J = 8.0 Hz, 2H), 7.92 (m, 1H), 7.88 (d, J = 8.4 Hz, 1H), 7.72 (s, 1H), 7.57–7.53 (m, 1H), 7.34–7.29 (m, 1H), 4.07–3.97 (m, 2H), 2.74–2.70 (s, 6H), 1.11 (t, 3H).

Ethyl 8-amino-2-(3-fluorophenyl)-1,7-naphthyridine-5-carboxylate. A mixture of ethyl 2-(2-cyano-6-(3-fluorophenyl)pyridin-3-yl)-3-(dimethylamino)acrylate (6.5 g, 19.15 mmol) and NH_4OAc (37 g, 478.84 mmol) in HOAc (60 ml) was heated at 80–100 °C overnight. The mixture was cooled to room temperature and poured into ice-water. The precipitate was collected and washed with ethanol (30 ml) to give the desired product, which was used directly in the next step (4.0 g, 67%). ^{1}H NMR (400 MHz, DMSO-*d6*) δ 9.21 (d, J = 8.8 Hz, 1H), 8.63 (s, 1H), 8.44 (d, J = 9.2 Hz, 1H), 8.43–8.40 (m, 1H), 8.23–8.21 (m, 2H), 8.04–8.00 (br, 1H), 7.57–7.53 (m, 1H), 7.32–7.29 (m, 1H), 4.32–4.27 (q, 2H), 1.34–1.31 (t, 3H).

8-Amino-2-(3-fluorophenyl)-1,7-naphthyridine-5-carboxylic acid. To a solution of ethyl 8-amino-2-(3-fluorophenyl)-1,7-naphthyridine-5-carboxylate (6.5 g, 20.88 mmol) in tetrahydrofuran/methanol/H_2O (10:2:1) (300 ml) was added NaOH (3.34 g, 83.5 mmol) at room temperature After the solution was stirred for 2 h at 65 °C, organic solvent was removed under reduced pressure and H_2O (50 ml) was added. The pH was adjusted to 8.0, the precipitate was collected by filtration and dried to give the desired product (5.9 g, 100%).

tert-Butyl 1-(cyclopropanecarbonyl)azetidin-3-ylcarbamate. To a mixture of cyclopropyl carboxylic acid (11.88 g, 138.01 mmol) in anhydrous dichloromethane (400 ml) was added diisopropylethylamine (44.59 g, 345.02 mmol) and HATU (*O*-(7-Azabenzotriazol-1-yl)-*N,N,N′,N′*-tetramethyluronium hexafluorophosphate; 52.47 g, 138.01 mmol). After the mixture was stirred at room temperature for 15 min, *tert*-butyl azetidin-3-yl carbamate trifluoroacetic acid salt (24.0 g, 115.01 mmol) was added and the reaction mixture was stirred at room temperature for another 3 h. The mixture was diluted by ethyl acetate, washed with saturated aqueous Na_2CO_3, saturated citric acid and brine. The organic layer was dried, concentrated, and purified by column to give the desired product (25.0 g, 90.5%). ^{1}H NMR (400 MHz, DMSO-*d6*) δ 7.58 (d, J = 7.6 Hz, 1H), 4.42 (t, J = 8.0 Hz, 1H), 4.34–4.26 (m, 1H), 4.03–3.99 (m, 2H), 3.67–3.64 (m, 1H), 1.52–1.46 (m, 1H), 1.38 (s, 9H), 0.71–0.65 (m, 4H).

(3-Aminoazetidin-1-yl)(cyclopropyl)methanone trifluoroacetic acid salt. To a solution of *tert*-butyl 1-(cyclopropanecarbonyl)azetidin-3-ylcarbamate (25.0 g, 104.04 mmol) in anhydrous dichloromethane (150 ml) was added trifluoroacetic acid (30 ml). After the reaction mixture was stirred at room temperature overnight, it was concentrated, and purified by column chromatography (10% CH_3OH in dichloromethane) to give the desired product (22.0 g, 89.1%). ^{1}H NMR (400 MHz, DMSO-*d6*) δ 8.19 (br, 3H), 4.50–4.46 (m, 1H), 4.19 (dd, J = 9.2, 3.2 Hz, 1H), 4.08–3.99 (m, 2H), 3.84–3.78 (m, 1H), 1.57–1.51 (m, 1H), 0.74–0.70 (m, 4H).

8-Amino-*N*-(1-(cyclopropanecarbonyl)azetidin-3-yl)-2-(3-fluorophenyl)-1,7-naphthyridine-5-carboxamide (GNE-495). To a solution of 8-amino-2-(3-fluorophenyl)-1,7-naphthyridine-5-carboxylic acid (500 mg, 1.77 mmol) in dimethylformamide (5 ml) were added PyBOP (benzotriazol-1-yl-oxytripyrrolidinophosphonium hexafluorophosphate; 1.10 g, 2.12 mmol) and diisopropylethylamine (456 mg, 3.53 mmol) at room temperature, followed by (3-aminoazetidin-1-yl)(cyclopropyl)methanone trifluoroacetic acid salt (297 mg, 2.12 mmol). After the mixture was stirred at room temperature overnight, it was poured into water, the solid was collected by filtration and washed with CH_3OH (10 ml) to give the desired product (400 mg, 56%). ^{1}H NMR (400 MHz, DMSO-d_6) δ 9.04–8.86 (m, 2H), 7.63–7.50 (m, 1H), 8.43 (d, J = 9.2 Hz, 2H), 8.34 (s, 1H), 8.25 (d, J = 8.1 Hz, 1H), 7.90–7.48 (m, 3H), 7.28 (td, J = 8.5, 2.6 Hz, 1H), 4.86–4.68 (m, 1H), 4.55 (t, J = 8.2 Hz, 1H), 4.24 (dd, J = 8.6, 5.3 Hz, 1H), 4.16 (t, J = 8.9 Hz, 1H), 3.89 (dd, J = 9.7, 5.5 Hz, 1H), 1.67–1.45 (m, 1H), 0.71 (dd, J = 7.9, 4.7, 4H). LC/MS (ESI+): m/z 406.4 ($M+H^+$).

32. Kisanuki, Y. Y. *et al.* Tie2-Cre transgenic mice: a new model for endothelial cell-lineage analysis *in vivo*. *Dev. Biol.* **230,** 230–242 (2001).
33. Seibler, J. *et al.* Rapid generation of inducible mouse mutants. *Nucleic Acids Res.* **31,** e12 (2003).
34. Connor, K. M. *et al.* Quantification of oxygen-induced retinopathy in the mouse: a model of vessel loss, vessel regrowth and pathological angiogenesis. *Nature Protocols* **4,** 1565–1573 (2009).
35. Nakatsu, M. N. *et al.* Angiogenic sprouting and capillary lumen formation modeled by human umbilical vein endothelial cells (HUVEC) in fibrin gels: the role of fibroblasts and angiopoietin-1. *Microvasc. Res.* **66,** 102–112 (2003).
36. Wilson, C. W. *et al.* Rasip1 regulates vertebrate vascular endothelial junction stability through Epac1-Rap1 signaling. *Blood* **122,** 3678–3690 (2013).
37. Ridgway, J. *et al.* Inhibition of Dll4 signalling inhibits tumour growth by deregulating angiogenesis. *Nature* **444,** 1083–1087 (2006).
38. Zaidel-Bar, R., Milo, R., Kam, Z. & Geiger, B. A paxillin tyrosine phosphorylation switch regulates the assembly and form of cell-matrix adhesions. *J. Cell Sci.* **120,** 137–148 (2007).
39. Bouaouina, M., Harburger, D. S. & Calderwood, D. A. *Talin and Signaling Through Integrins* Vol. **757,** Ch. 20, 325–347 (Humana Press, 2011).
40. Lad, Y., Harburger, D. S. & Calderwood, D. A. *Integrin Cytoskeletal Interactions* Vol. 426, 69–84 (Elsevier, 2007).
41. Pfaff, M., Liu, S., Erle, D. J. & Ginsberg, M. H. Integrin beta cytoplasmic domains differentially bind to cytoskeletal proteins. *J. Biol. Chem.* **273,** 6104–6109 (1998).
42. Berginski, M. E. & Gomez, S. M. The Focal Adhesion Analysis Server: a web tool for analyzing focal adhesion dynamics. *F1000Res.* **2,** 68 (2013).
43. Bentley, K. *et al.* The role of differential VE-cadherin dynamics in cell rearrangement during angiogenesis. *Nature Cell Biol.* **16,** 309–321 (2014).
44. Schreiner, C. L. *et al.* Isolation and characterization of Chinese hamster ovary cell variants deficient in the expression of fibronectin receptor. *J. Cell Biol.* **109,** 3157–3167 (1989).

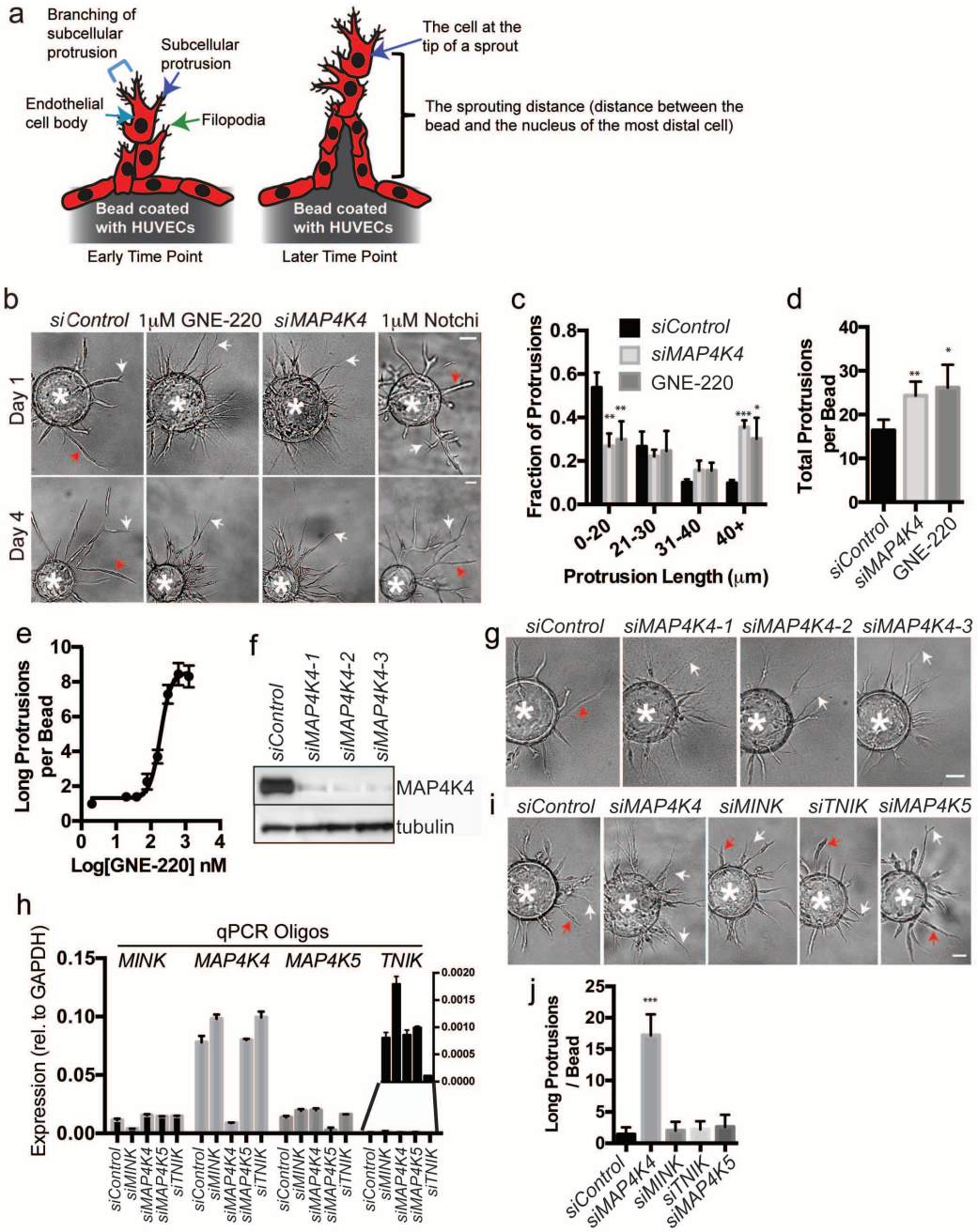

Extended Data Figure 1 | The roles of a subset of MAP4Ks and Notch in the HUVEC sprouting assay. **a**, A diagram illustrating the cellular and sub-cellular structures in the three-dimensional (3D) culture of HUVECs coated on beads[35]. A sprout refers to the multi-cell structure that resembles a capillary. These sprouts grow out of the HUVECs coated on the surface of the plastic beads, and their length increased over time. The structures associated with each individual endothelial cell in this culture system are indicated on the diagram. Subcellular protrusions are membrane structures between 5 and 10 μm in width and are irregularly shaped. Filopodia are significantly thinner than subcellular protrusions (<1 μm) and are linear. **b**, Representative bright field images of HUVEC sprouts treated with the indicated siRNA, GNE-220, or a Notch pathway inhibitor DBZ (Notchi) after 1 and 4 days in culture. These images were taken from similar cultures that generated data presented in Fig. 1a. These figures showed the two types of images we used to monitor and quantify HUVEC sprouting behaviours. Unlike *siMAP4K4* or GNE-220, DBZ did not increase subcellular protrusions and accumulation of aberrant structures near the beads; instead, it increased branching of capillary-like sprouts. **c**, Distribution of subcellular protrusion lengths in the HUVEC sprouting assay after 1 day in culture. Treatment with *siMAP4K4* or GNE-220 significantly increased the number of subcellular protrusions longer than 40 μm. Data represent means from 4 experiments. **d**, The number of total subcellular protrusions per bead from the same experiments as **b**. **e**, Dose–response curve relating the number of long protrusions (>40 μm) to GNE-220 concentration after 24 h with inhibitor treatment. $n = 4$ independent cultures. **f**, Western blot analysis showing *MAP4K4* knockdown efficiency in HUVEC for three independent siRNAs 72 h after transfection. **g**, Representative bright field images of HUVEC sprouts after 1 day in culture with *MAP4K4* knockdown using three independent siRNA. **h**, Quantitative PCR measuring mRNA levels of four closely related human *MAP4K* genes after knockdown with the indicated siRNA pools. Knockdown of *MAP4K4* does not affect other kinases. **i**, Representative bright field images of HUVEC sprouts after knockdown with the indicated siRNA after 1 day in culture. In **b**, **g** and **i**, red arrows indicate sprouts consisting of cell bodies, white arrows indicate subcellular membrane protrusions, and asterisks indicate beads coated with HUVEC. **j**, Quantification of experiment shown in **i** showing only *MAP4K4* knockdown results in increase of long protrusions (>40 μm). Scale bars, 50 μm. For all extended figures: error bars represent standard error of the mean (s.e.m.); statistical significance between the indicated sample versus control, or the marked pairs are: $*P < 0.05$, $**P < 0.01$, $***P < 0.001$, or NS ($P \geq 0.05$) by statistical analysis described in the Methods.

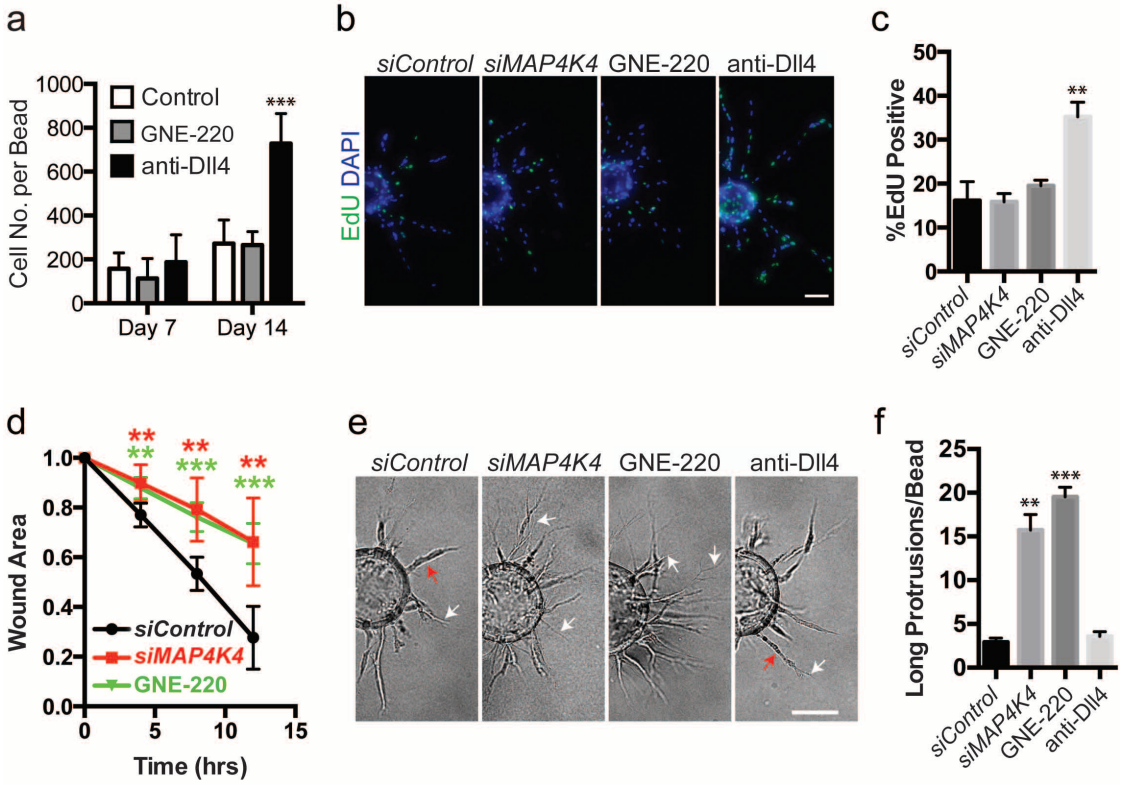

g

Filopodia Measurements	*siControl*	*siMAP4K4*
Growth Rate (μm/sec)	0.21 ± 0.05	0.26 ± 0.03
Number (number/μm)	0.054 ± 0.013	0.054 ± 0.012
Length (μm) *	15.3 ± 1.2	12.7 ± 1.2
Cycle Time (sec)	496 ± 204	423 ± 150

Extended Data Figure 2 | The roles of MAP4K4 and Dll4-Notch in regulating HUVEC proliferation, migration, and subcellular structures in the HUVEC sprouting assay. **a**, Quantification of HUVEC nuclei number per bead in the 3D culture at the indicated time points in the presence or absence of GNE-220 or anti-Dll4 antibody. While inhibition of Notch-Dll4 signalling increased cell number, GNE-220 had no significant effect. $n = 16$ beads per condition. Representative of 4 experiments. **b**, Representative images of HUVEC sprouts stained with DAPI (blue) and EdU (green). After 4 days in culture, cells were incubated with EdU for 16 h before staining and imaging. **c**, Quantification of percentage of nuclei that score as EdU positive. $n = 4$ experiments. **d**, Wound area as a function of time in the HUVEC scratch wound healing assay treated with control siRNA, *siMAP4K4* or GNE-220. $n = 6$ independent cultures. **e**, Representative images of HUVEC sprouts after 1 day in culture with the indicated treatments. *siMAP4K4* and GNE-220 increased long subcellular protrusions but anti-Dll4 had no effect on these structures. Red arrows indicate sprouts, white arrows indicate protrusions. **f**, Quantification of images shown in **e**. $n = 3$ experiments. **g**, Quantification of filopodia number and dynamics in HUVEC sprouts from experiments described in Supplementary Video 3. Scale bars, 100 μm.

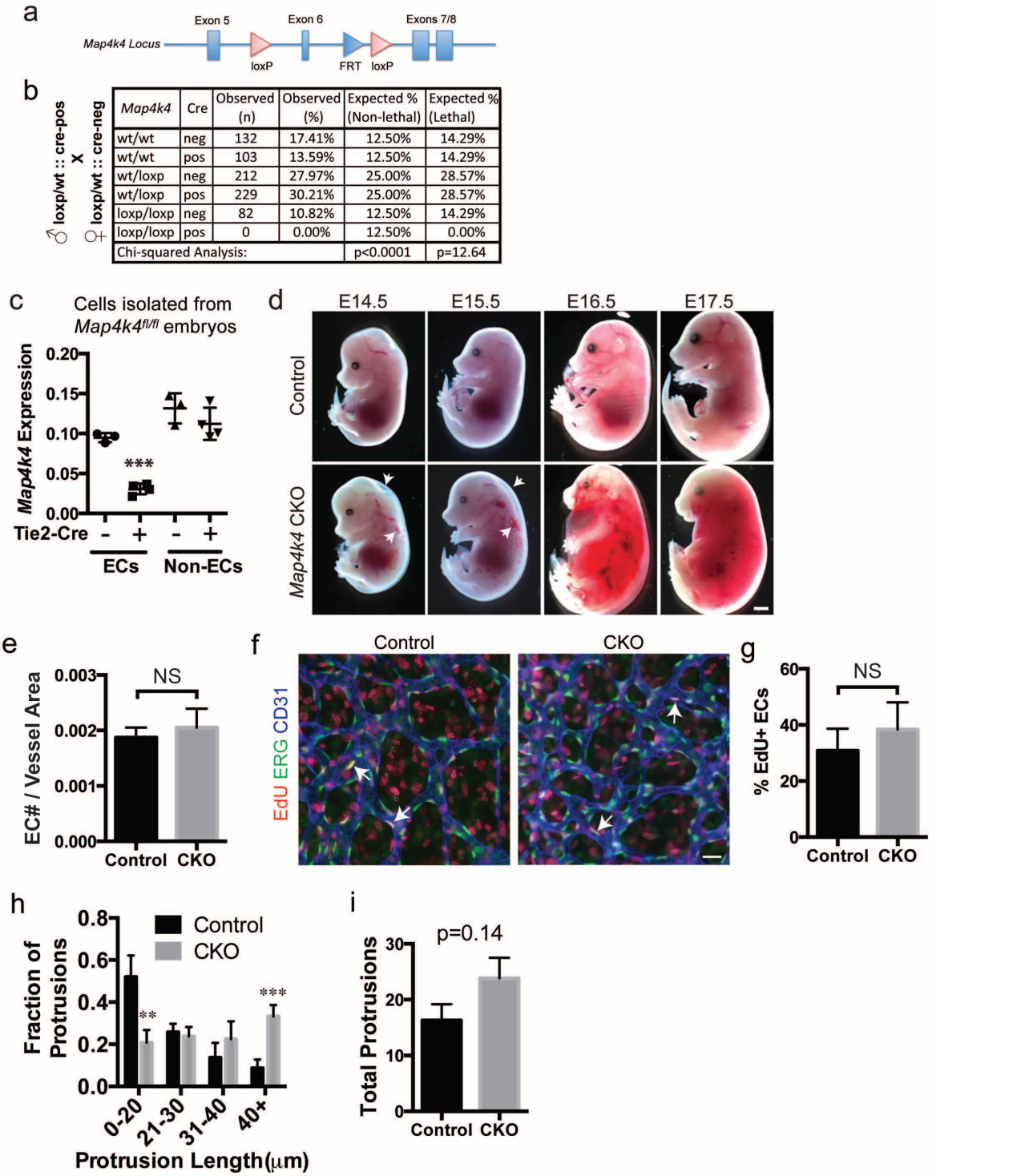

Map4k4	Cre	Observed (n)	Observed (%)	Expected % (Non-lethal)	Expected % (Lethal)
wt/wt	neg	132	17.41%	12.50%	14.29%
wt/wt	pos	103	13.59%	12.50%	14.29%
wt/loxp	neg	212	27.97%	25.00%	28.57%
wt/loxp	pos	229	30.21%	25.00%	28.57%
loxp/loxp	neg	82	10.82%	12.50%	14.29%
loxp/loxp	pos	0	0.00%	12.50%	0.00%
Chi-squared Analysis:				p<0.0001	p=12.64

Extended Data Figure 3 | Additional characterizations of *Map4k4* conditional knockout mice. **a**, Schematic representation of the *Map4k4* floxed allele used in this study. When this floxed allele is present in cells expressing Cre, recombination results in the deletion of sequence encoding the MAP4K4 catalytic domain and introduces a stop codon at amino acid 144. If the truncated protein (amino acids 1–144) could be translated, it is expected to be non-functional and probably unstable. **b**, Summary of genotypes detected from progenies of the indicated cross. Genotype distribution is consistent with embryonic lethality based on Chi-squared analysis. *P* value indicates the probability of obtaining a distribution similar to the expected distributions for lethality or non-lethality. **c**, Quantitative RT–PCR analysis of *Map4k4* normalized to *mRPS13* in isolated endothelial cells and non-endothelial cells from *Map4k4*$^{fl/fl}$::Tie2-Cre positive (+) embryos versus *Map4k4*$^{fl/fl}$::Tie2-Cre negative (−) littermates. $n = 3$–4 embryos per genotype. **d**, *Map4k4* CKO embryos and wild-type littermates harvested at the indicated stages. Arrows indicate focal haemorrhage and oedema. Scale bar, 1 mm. **e**, Quantification of ERG-positive endothelial cell nuclei normalized to vascularized areas in E14.5 head skins derived from control or CKO embryos. $n = 7$ control embryos, 4 CKO embryos. **f**, Representative confocal images of E14.5 embryonic head skin after 4 h labelling with EdU. Vessels stained with CD31 (blue), endothelial cell nuclei stained with ERG (green), proliferating nuclei marked as EdU positive (red). White arrows indicate proliferating endothelial cells. **g**, endothelial cell proliferation in the embryonic head skins were quantified as % of EdU$^+$ cells in all ERG$^+$ cells. $n = 9$ control embryos, 7 CKO embryos. **h**, Fraction of membrane protrusions along the vascular front with indicated lengths in control and CKO embryonic head skins. $n = 3$ animals per genotype. Asterisks indicate statistics between control and CKO. **i**, Total number of protrusions along the vascular front in control and CKO head skins per mm vascular front. $n = 3$ animals per genotype.

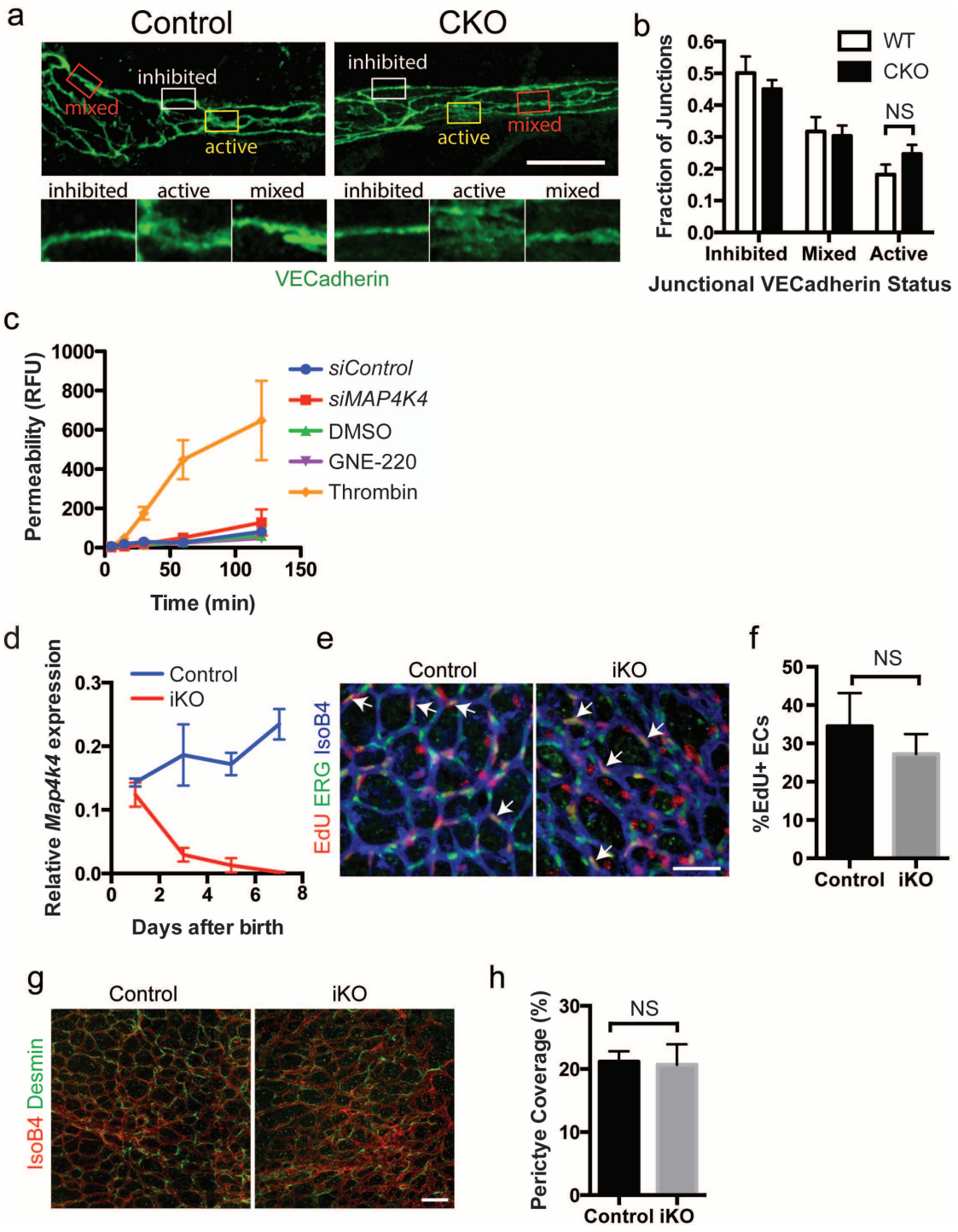

Extended Data Figure 4 | Additional characterizations of *Map4k4* conditional and inducible knockout mice. **a**, Confocal images of E14.5 head skin vasculature stained with VE-Cadherin in control and CKO embryos. Bottom panels are enlarged view of the boxed areas. **b**, Quantification of endothelial cell junction morphology in control and CKO animals shown in panel **a**. As defined in Bentley *et al.*[43], the "active" junction refers to diffused or serrated junction that reflects junctional remodelling, the "inhibited" morphology refers to linear junctions that reflect relative junctional stability, and the "mixed" junction contains both morphologies within the defined length. $n > 13$ regions per group, 2 embryos per genotype. Scale bars represent 12 µm. **c**, Permeability of confluent HUVEC monolayers with the indicated treatments was measured by FITC-dextran trans-well diffusion over time. $n = 3$ experiments. **d**, Quantitative RT–PCR results depicting *Map4k4* expression levels relative to *mRPS13* as a function of time after birth for control and iKO animals. Pups were injected with 80 mg per kg (body weight) tamoxifen once daily starting on P1, and mRNA were isolated and measured from tail clips on P3, P5, and P7. $n = 4$ control mice, 6 iKO mice for all time points. **e**, Representative confocal images of P7 retinal vasculature 16 h after EdU injection. Vessels stained with IsoB4 (blue), endothelial cell nuclei stained with ERG (green), proliferating nuclei marked as EdU positive (red). Arrows indicate EdU^+ endothelial cells. **f**, Quantification of EdU^+ endothelial cells normalized to total ERG^+ cells in the retina. $n = 5$ control animals, 6 iKO animals. **g**, Representative confocal images of control and iKO retina on P7 stained with desmin to highlight pericytes (green) and IsoB4 to indicate endothelial cells (red). **h**, Quantification of pericyte coverage from experiments shown in **d**. $n = 6$ animals per genotype. Scale bars in **e** and **g**, 50 µm.

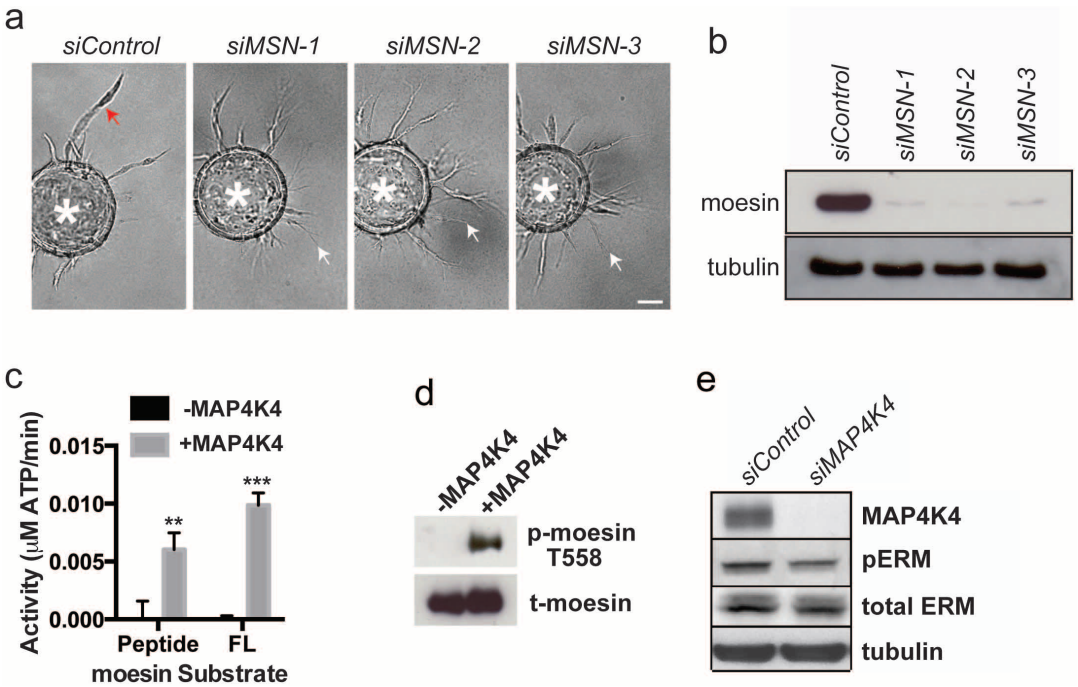

Extended Data Figure 5 | HUVEC sprouting assay with individual *MSN* siRNAs and MAP4K4 kinase activity on moesin. **a**, Representative bright field images of HUVEC bead sprouts transfected with three independent siRNA targeting *MSN* after one day in culture. Red arrows indicate sprouts consisting of cell bodies, white arrows indicate subcellular protrusions, and asterisks indicate beads coated with HUVEC. Scale bar, 50 μm. **b**, Western blot confirmed knockdown of *MSN* 72 h after transfection with three independent siRNAs. **c**, ATP consumption rates of recombinant activated MAP4K4 kinase domain against full-length moesin or a peptide corresponding to amino acids surrounding T558 in moesin. **d**, Western blot of reaction products from **c** showing moesin phosphorylation at T558. t, total. **e**, Western blot of the indicated total and phosphorylated (p) proteins from HUVEC transfected with the indicated siRNA. $n = 3$ experiments.

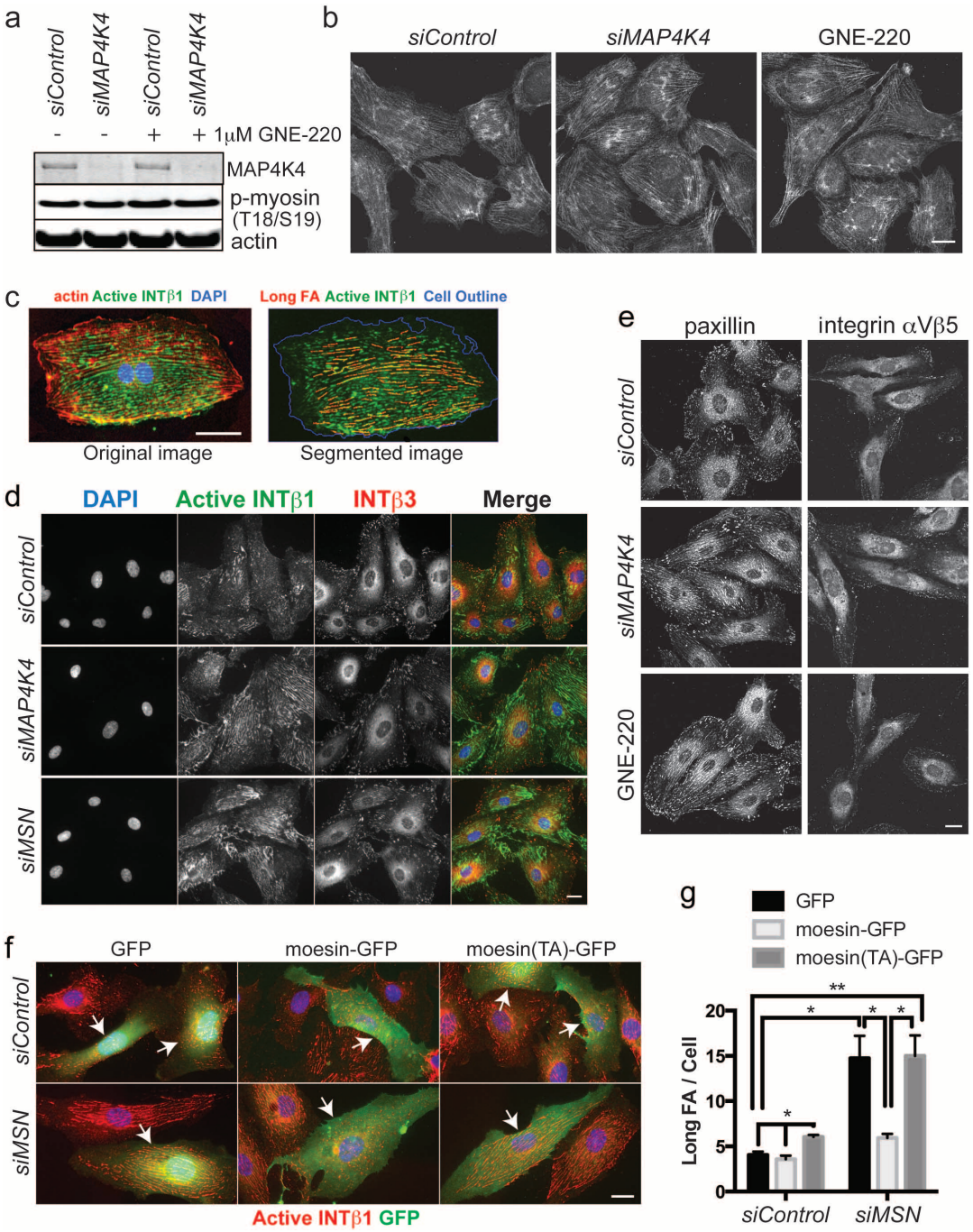

Extended Data Figure 6 | The roles of MAP4K4 and moesin on myosin and focal adhesions. **a**, Western blot analysis of HUVEC lysates 72 h after transfection with *MAP4K4* siRNA with (+) or without (−) 24 h treatment with GNE-220. **b**, Representative images of HUVEC treated with *siMAP4K4* or GNE-220 and stained with p-myosin. **c**, A representative image of HUVEC stained with phalloidin to highlight actin (red), active INTβ1 (green), and DAPI (blue) (left). Right, automated segmentation of long focal adhesions (red) overlaying on top of active INTβ1 staining (green) and the outline of the cell (blue). **d**, Epifluorescent images of HUVEC transfected with the indicated siRNA pools. Active β1 (green) and β3 (red) integrins mark mature and nascent focal adhesions, respectively. DAPI staining is shown in blue. **e**, Confocal images of HUVEC treated with control siRNA, *siMAP4K4* or GNE-220 and stained with paxillin (left) and integrin αVβ5 (right). **f**, Epifluorescent images of HUVEC transfected with control siRNA or siRNA targeting the 3′ UTR of *MSN*. siRNA-treated cells were electroporated with constructs expressing GFP, or GFP-tagged wild-type moesin or moesin(T558A) (green) and stained with active INTβ1 antibody (red). Arrows indicate cells expressing GFP or GFP-tagged proteins. **g**, Quantification of long FAs in GFP positive cells shown in **f**. Interestingly, expression of the moesin(T558A) construct moderately increased long FAs, indicating that this construct may have weak dominant negative activity. $n = 3$ experiments for all panels. Scale bars, 10 μm.

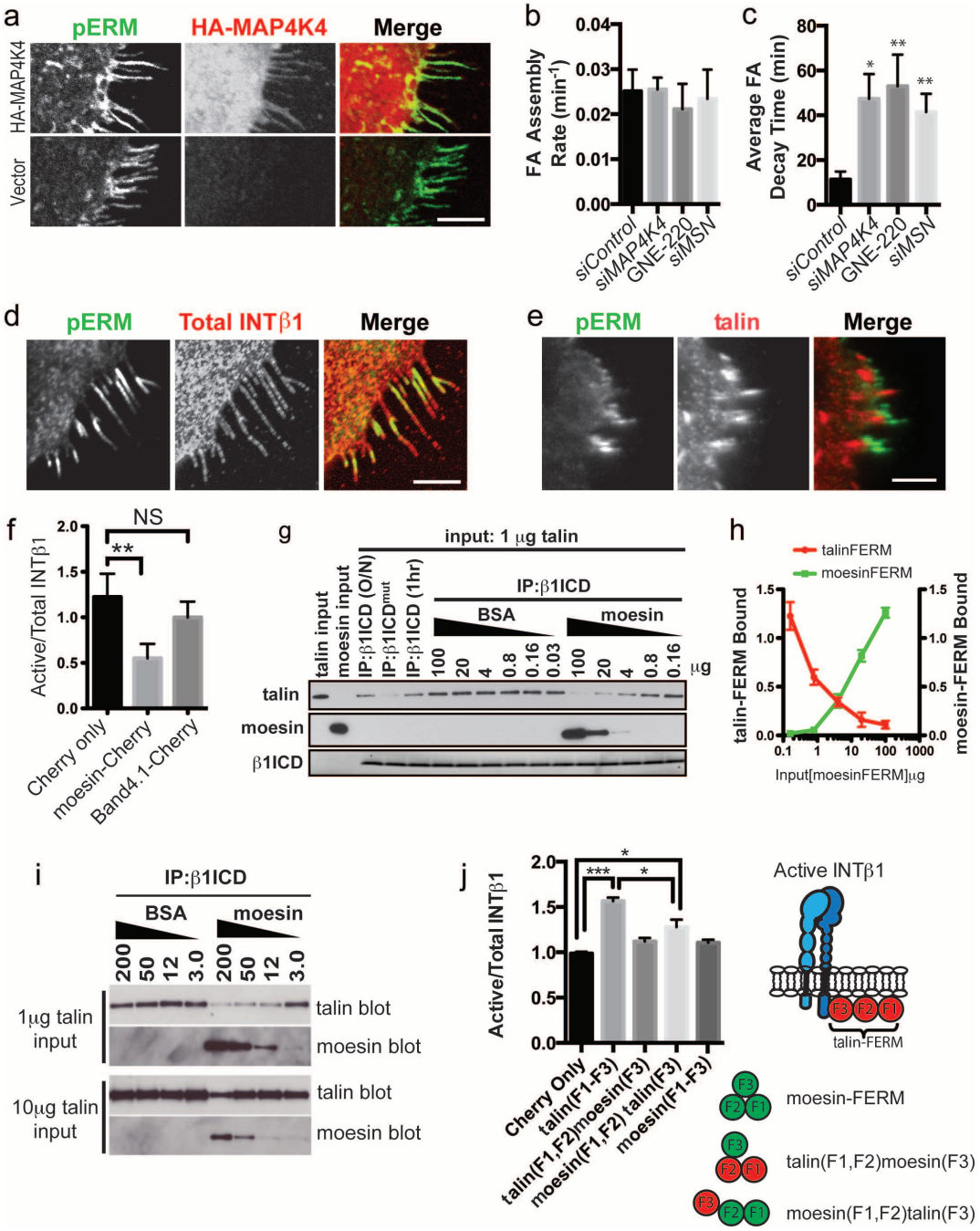

Extended Data Figure 7 | Further characterizations of MAP4K4 and moesin in retraction fibres, FA dynamics, and integrin activity. **a**, Confocal images of retraction fibres in HUVEC infected with empty viral vector (bottom) or viral construct expressing HA-MAP4K4 and stained with anti-HA antibody (red) and pERM (green). We evaluated 13 commercially available anti-MAP4K4 antibodies in HUVECs with and without *siMAP4K4*, but failed to identify any antibody that specifically stained MAP4K4 on cells. Overexpressed MAP4K4 was then used to evaluate its distribution. **b**, **c**, FA assembly rates (**b**) and average FA decay time (**c**) in HUVEC expressing paxillin–GFP. Quantification was done using the Focal Adhesion Analysis Server (http://faas.bme.unc.edu/). $n = 8$ videos per condition. **d**, TIRF images of retraction fibres in HUVEC stained with total INTβ1 (red) and pERM (green). **e**, TIRF images of retraction fibres in HUVEC stained with pERM (green) and talin (red). **f**, FACs analysis of active and total INTβ1 in CHO cells expressing mCherry alone, mCherry-tagged moesin FERM domain, or mCherry-tagged Band4.1 FERM domain. Each bar represents the mean of more than 3 independent pools of CHO cells transfected with the indicated constructs. Integrin activation in this experiment relied on endogenously expressed Talin. **g**, Recombinant wild-type or mutant integrin β1ICD coated beads were incubated with talin for one hour (1 h) except the sample labelled O/N (overnight, lane 3 from the left), followed by the addition of the indicated competitor proteins. The pulled-down or input proteins were analysed by western blotting. Comparison between lanes 3 and 5 indicates that one-hour incubation allowed maximal talin binding with integrin β1ICD similar to overnight incubation. IP, immunoprecipitation. **h**, Quantification of talin and moesin associated with β1ICD-coated beads in the presence of increasing concentrations of moesin. $n = 3$ experiments. **i**, Talin and moesin at the indicated quantities were co-incubated with beads coated with INTβ1ICD. The immunoprecipitated proteins were analysed by western blotting. Increased talin input reduced moesin binding to β1ICD, suggesting that talin competes with moesin for binding to β1ICD. **j**, FACs analysis of active and total INTβ1 in CHO cells expressing mCherry alone, mCherry-tagged wild-type talin or moesin FERM domain, or the indicated mCherry-tagged talin-moesin chimaeric FERM domain. To avoid the confounding effect of moesin-FERM's inhibitory activity, we gated for cells with low FERM expression where moesin-FERM was insufficient to inhibit INTβ1. Cells expressing the same levels of mCherry were gated and analysed for total and active INTβ1. $n = 3$ experiments. Scale bars, 5 μm.

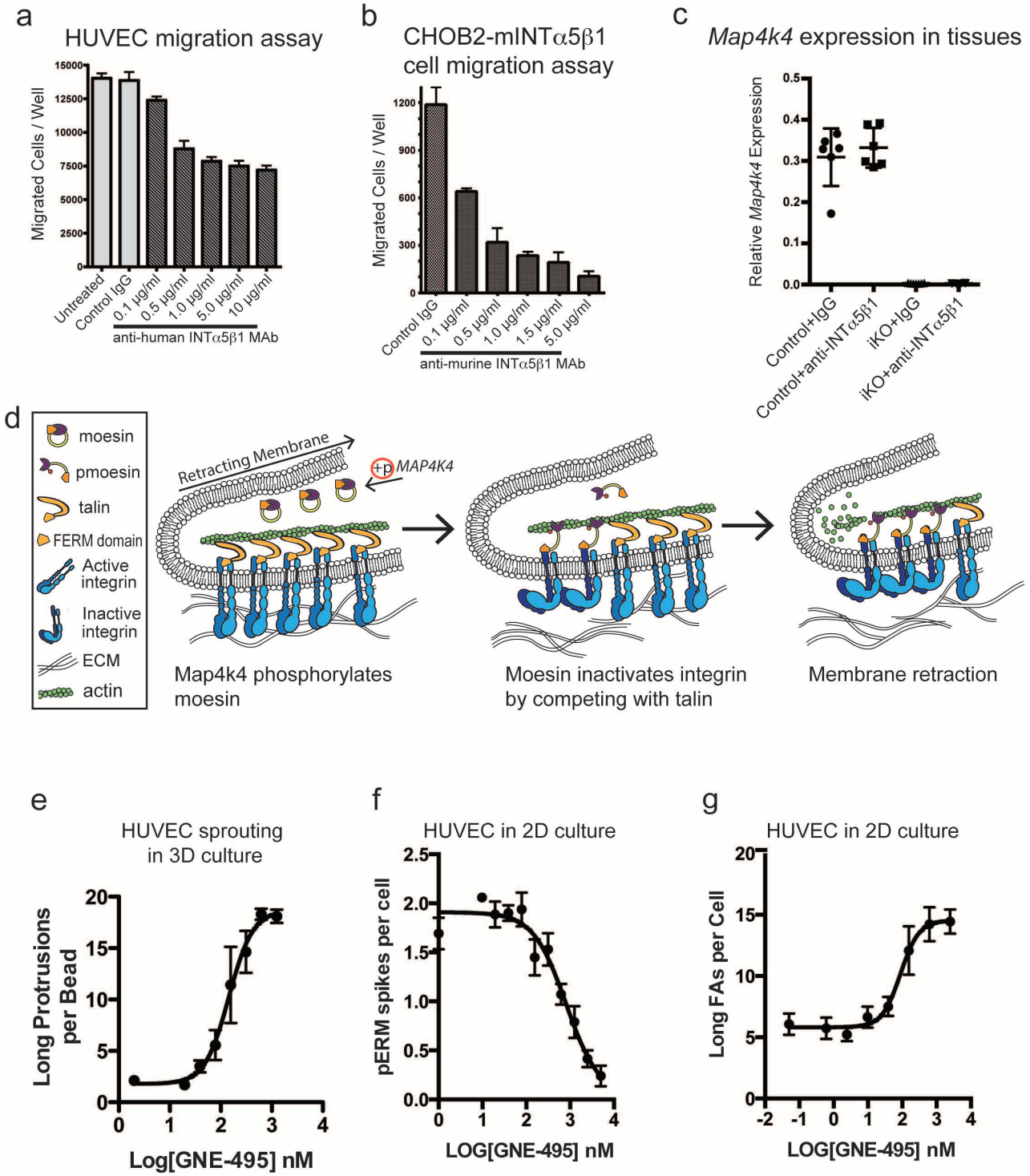

Extended Data Figure 8 | Additional information about the integrin-α5β1 antibodies, MAP4K4 inhibitor GNE-495, and a model depicting how MAP4K4 and moesin regulate FA disassembly. **a**, HUVEC migration assay results plotted as number of cells migrated through the membrane (*y*-axis) versus the concentrations of antibodies (*x*-axis). The graph shows that the anti-human INTα5β1 MAb 18C12 dose dependently inhibited migration of HUVECs on fibronectin. **b**, CHOB2-mα5β1 cells migration assay results plotted as number of cells migrated through the membrane (*y*-axis) versus the concentrations of antibodies (*x*-axis). The graph shows that the anti-murine INTα5β1 monoclonal antibody 10E7 dose-dependently inhibited migration of CHOB2-mα5β1 on fibronectin. Data presented in **a** and **b** were derived from 6 independent samples per condition. Detail information about MAbs 18C12 and 10E7 can be found in the Methods. Note that since HUVEC expressed several fibronectin receptors, inhibition of migration by an anti-α5β1 MAb was partial even at high MAb concentrations, whereas CHOB2 cells are deficient for many integrins[44], inhibition of CHOB2-mα5β1 cells migration by an anti-α5β1 MAb was more profound. **c**, Quantitative PCR measurement of *Map4k4* normalized to *mRPS13* using cDNA from neonatal tail clips of P7 mice with the indicated *Map4k4* genotypes (control or iKO) after injection with tamoxifen and the indicated antibodies. **d**, Model for MAP4K4 regulation of membrane retraction. Upon phosphorylation by MAP4K4, the FERM domain of activated moesin competes with talin-FERM for binding to active integrin, leading to integrin inactivation and FA disassembly. These events promote efficient membrane retraction to enable cell migration. Additional FA components omitted for simplicity. **e**–**g**, Characterization of the MAP4K4 selective inhibitor GNE-495: dose response curves relating GNE-495 concentration to long membrane protrusions in HUVEC bead sprouting assay (**e**), pERM-positive spikes (**f**), and long FAs in 2D HUVEC culture 24 h after GNE-495 treatment (**g**). Data represent average of 4 independent cultures.

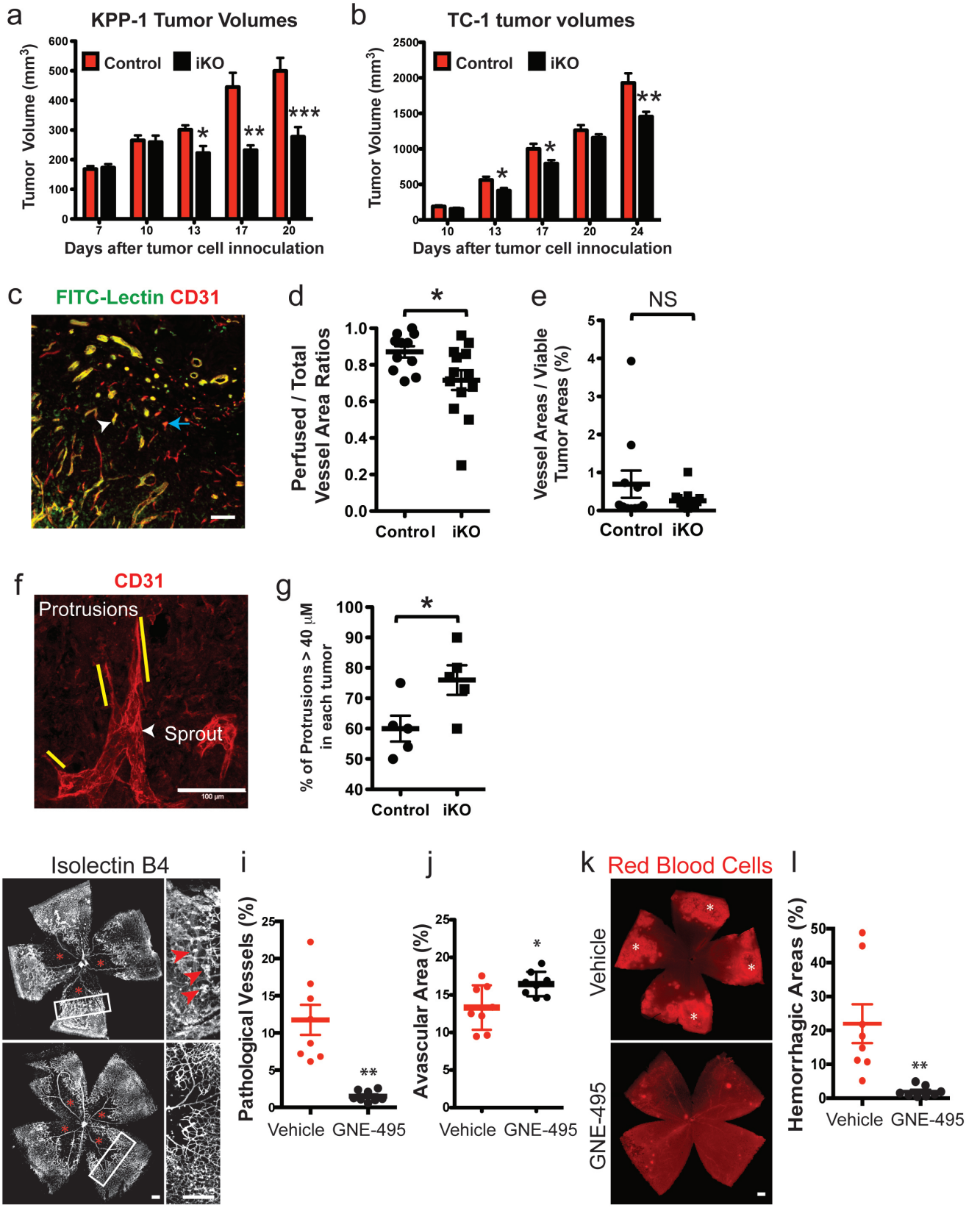

Extended Data Figure 9 | The role of MAP4K4 in pathologic angiogenesis. **a**, **b**, Murine pancreatic (KPP-1) and lung (TC-1) cancer cells were implanted subcutaneously in control and *Map4k4*$^{iKO/iKO}$ sibling mice. Mean volumes of KPP-1 tumours from 10 mice per genotype (**a**) and TC-1 tumours from 15 mice per genotype (**b**) were measured over time. Per IACUC guidance, at the later time points, mice with tumour volumes exceeding 1,000 mm^3 (KPP-1) or 2,500 mm^3 (TC-1) were euthanized and no longer included in the mean tumour volume calculation. On day 20 for the KPP-1 study: $n = 9$ for the control group, $n = 10$ for the iKO group. On day 24 for the TC-1 study: $n = 11$ for the control group, $n = 14$ for the iKO group. **c**, Representative confocal image of a KPP-1 tumour section stained with FITC-lectin (green), CD31 (red) to indicate how functional vessels were analysed. White arrowhead indicates a perfused vessel (double positive for FITC-lectin and CD31, shown as yellow), blue arrow indicates a non-perfused vessel (single positive for CD31). **d**, Quantification of perfused tumour vessels on whole tumour sections from the KPP-1 model. Each dot represents the mean value of an entire tumour from a mouse. **e**, Quantification of tumour vessel areas normalized to the viable tumour areas on whole tumour sections from the KPP-1 model revealed no significant change in tumour vascular density in the iKO host. Each dot represents the mean value of an entire tumour from a mouse. **f**, Representative confocal projection image of a KPP-1 tumour thick section stained with CD31 to indicate how long subcellular protrusions were analysed. Arrow indicates a sprout, yellow lines indicate the subcellular protrusions. **g**, Quantification of long protrusions in each tumour. Each dot represents the mean value of multiple micrographs from the tumour of one mouse. A total of 170 protrusions were analysed. Scale bars represent 100 μm for **c** and **f**. Regarding **e**, the lack of significant change in tumour vascular density is not surprising as we observed a delay in vascularization balanced by the accumulation of endothelial cells in the already vascularized areas (Figs 2b, f, 6b), resulting in a lack of overall density change. Decreased perfusion may reflect the blood vessel structural alteration due to the aforementioned endothelial cell accumulation (Fig. 1a red arrowheads). **h–l**, Effects of the MAP4K4 inhibitor GNE-495 was evaluated in an oxygen-induced retinopathy (OIR) model that mimics vascular pathologies in human proliferative diabetic retinopathy and retinopathy of prematurity. **h**, Confocal images of P17 retinas stained for isolectin-B4 from mice subjected to the OIR procedure and treated with either vehicle or GNE-495. Red asterisks mark areas of vaso-obliteration (avascular area) resulting from high oxygen damage. Right, close-up views of the boxed areas. Red arrows mark pathologic vascular tufts. **i**, Areas of pathologic vascular tufts normalized to retinal areas. Control retinas contain numerous pathological neovascular tufts, which is largely absent from the GNE-495 treated retinas, revealing the inhibitory effect of GNE-495 on pathologic angiogenesis. **j**, Avascular areas normalized to retinal areas. GNE-495 increased avascular area, indicating an inhibition of vascular regrowth into the oxygen damaged avascular area. **k**, Autofluorescence of red blood cells indicative of haemorrhage (white asterisks) in retinas from the same experiment shown in **h**–**j**. **l**, Haemorrhagic areas normalized to retinal area illustrates that GNE-495 reduced haemorrhage. Each dot represents one animal. Scale bar, 50 μm.